Investigations of Single Longitudinal Mode and Frequency Stability in Standing Wave and Unidirectional Cavity Lasers

Karl Åkerblom

Abstract

The purpose of this thesis was to investigate the mode structure and frequency tuning of a number of continuous wave diode pumped solid state laser platforms with varied cavity designs and packaging. One of the goals of the investigation was to determine if the lasers always outputted single longitudinal mode or if side modes would appear under certain conditions for the environment or laser. The thesis was also concerned with the drifts in output frequency under different conditions for the environment and laser. The tested lasers were subjected to changing environmental temperature by mounting the lasers on a temperature controlled base plate. During the later parts of the testing phase, some lasers were also subjected to varying temperature of internal components using built-in temperature controls, to determine the possibilities of active management of mode structure and frequency tuning by adjusting settings inside the laser in response to changes in output. During all tests the output of the lasers were monitored using a wavemeter to determine absolute frequency for the strongest mode, and a Fabry Perot interferometer was used to determine the mode structure as well as relative frequency change of the strongest mode.

The thesis begins with three introductory sections, detailing the background and purpose in Section 1, followed by Section 2; an overview of theoretical concepts in optics and laser physics touched in this thesis. Thirdly Section 3 details the equipment and methodology used during the tests. The thesis proceeds with the measurement results in section 4, divided into three subsections; first results from tests with varying base plate temperature, then results from tests with constant base plate temperature and finally measurement results with varying temperatures for internal components of the lasers. The thesis concludes with Section 5 & 6, where conclusion and suggestions for future work are presented.

Acknowledgments

I would like to thank Jonas Hellström and Håkan Karlsson for giving me the opportunity to do my thesis at Cobolt AB. Jonas input, guidance and numerous proof readings has also been a tremendous help. I would like to thank the whole R&D department for all their assistance with answering my many questions, and I would like to extend a special thanks to Gunnar Elgcrona for his generous sharing of insights and knowledge about laser physics and laser design. I wish to thank the Production department at Cobolt for their various help during the lab work of this thesis, and I would like to extend a special thanks to Olga Vlassova for her patience and kindness during the months when I would at least once daily require her help with acquiring test equipment and lasers.

I wish to express my utmost gratitude to my mother and father for their support and inspiration. It would be futile to even attempt a list of the myriad of ways that you have helped me reach this point, I can only extend all my thanks.

Lastly I wish to thank my friends for supplying encouragement and distraction in good proportion. A special thanks to Alexander Ludkiewicz, Johan Wiktorsson and Maria Jörle for their great encouragement and advisement during the work on this thesis.

Contents

List of Figures

List of Tables

1 Introduction

1.1 Background

Cobolt is a Swedish photonics company specialized in the development and manufacture of diode and solid-state lasers with high requirements on robustness and spectral quality. The lasers built at Cobolt are used in a wide variety of applications including biomedical imaging, holography, interferometry, Raman spectroscopy etc. Some of these applications require a high spectral purity of the laser source in order to achieve the best possible result. For instance; Raman spectroscopy is based on measurements of in-elastically scattered light from samples illuminated by laser light, and in order to observe clearly resolved peaks in the scatter-spectrum we require the laser light to be monochromatic with a stable wavelength and narrow linewidth.

Cobolt has two main product families of diode pumped solid-state lasers, one based on a standing-wave resonator and the other based on a unidirectional ring cavity. The lasers utilize non-linear optical components to perform frequency mixing of the laser light, generating the output light. In order to achieve high spectral purity in the output, spectral filters are sometimes included in the cavity to help the solid-state laser to oscillate on a single mode. Preferably the lasers should be able to withstand large temperature changes of the surrounding environment and still remain single mode, with minimal changes in wavelength.

1.2 Purpose

The purpose of this master thesis is to investigate the spectral purity and stability of the two cavity types. By controlling the temperature of a base plate that the laser is mounted on and measuring the spectral structure of the output light, we wish to determine how the frequency and mode structure of the output changes with temperature. Is the output always single mode? How does the frequency change, in discrete jumps or continuously? How stable is the output when base plate temperature is held constant? Is it possible to adjust settings in the lasers in order to counteract the impact of changes in the surrounding environment? How do these characteristics differ between standing-wave resonator lasers and unidirectional ring resonator lasers?

2 Theory

2.1 Laser introduction

2.1.1 Stimulated emission and population inversion

The heart of any laser consists of a so called gain medium. The purpose of the gain medium is to amplify light as it travels through the medium. This is performed using an interaction between photons and electrons in the medium known as stimulated emission; as a photon with energy $E_p = h\nu$ travels near an electron in an excited energy state with energy E_2 it is possible for the two to interact, causing the electron to transition to a lower energy state E_1 while emitting a photon with the same phase, energy and directionality as the impinging photon. The requirement for this exchange of energy to take place is that the difference between energy levels $E_2 - E_1 = E_p$.

As light with energy E_p travels through the gain medium it will encounter electrons in both state E_1 and E_2, and so will undergo stimulated emission but also absorption, where the photon is absorbed by the electron and the electron gets excited from state E_1 to E_2. To achieve any meaningful amplification it would stand to reason that photons would have to encounter more electrons in the higher energy state of E_2 than lower state E_1 as they pass through the gain medium. But Boltzmann statistics tells us that in thermal equilibrium the populations of the two levels(N_1, N_2) can be described as

$$\frac{N_2^e}{N_1^e} = exp[\frac{-(E_2 - E_1)}{kT}] \tag{1}$$

and since $E_2 > E_1$this means that $N_1^e > N_2^e$.

If we want amplification in the gain medium we have to manipulate the populations such that $N_2 > N_1$, and this is known as achieving population inversion. It is performed by supplying energy to the medium in such a way that a large population is deposited in E_2 without increasing the population in E_1 and is referred to as pumping the medium. Pump mechanisms take many different forms and implementations but the simplest strategy consists of exciting electrons from E_1 to a state E_3 from which it quickly and spontaneously transitions to our preferred state E_2 , eventually resulting in population inversion with sufficient pumping. This is referred to as having a three level laser. Some gain mediums also take advantage of a lower energy state E_0, so that electrons in state E_1 quickly and spontaneously transition to E_0, where it can be pumped to E_3. This depletes E_1 and vastly reduces the effort necessary to achieve population inversion between E_1 and E_2. This is referred to as having a four level laser. For all lasers in this thesis the gain medium consists of a Nd:YAG crystal that behaves like a four level laser and gets pumped by focusing a diode laser beam into the crystal.

2.1.2 Oscillation and outcoupling

Once we have a gain medium that allows us to amplify light on pass, we would like to repeat this process many times over. This is performed by placing the gain medium in an oscillation cavity, made with highly reflective mirrors that direct the light in a closed path passing through the medium. In its simplest form the cavity simply consists of two mirror placed on opposite sides of the gain medium but it is also possible to build circular cavities that direct the light around in some form of loop.

The oscillation cavity allows a field to build up with increasing intensity until an equilibrium between gain and loss is achieved within. By using a slightly lower reflectance on one of the cavity mirrors it is possible to outcouple the field, allowing a fraction of the laser light to exit the cavity. For most implementations this is how the output of the laser

is accessed. However, all the lasers in this thesis (with the exception of one) use the oscillating laser light to produce light of double the frequency (by a process, second harmonic generation, that we will discuss shortly) as output, which means that the lasers have no need to directly outcouple the fundamental field built up inside the cavity. Rather, these lasers are built to only emit the frequency doubled light out of the cavity.

2.2 Modes in laser operation

2.2.1 Laser linewidth and line-broadening

In the basic description of laser operation, a population inversion between two energy levels is generated in the lasing medium by some form of pump mechanism, and light with energy corresponding to the difference in energy between the two levels experiences amplification as a result of stimulated emission. This would seem to suggest that only light with the specific transition energy ($E_p = h\nu = E_2 - E_1$) experiences stimulated emission when passing through the lasing medium. In actual fact, all laser mediums support absorption and stimulated emission over a non-zero range of frequencies surrounding the transition frequency. The spectral line profile that describes how likely photons are to interact with the transition is usually a Lorenzian or Gaussian shape centered on the transition frequency with a width referred to as the linewidth of the transition.

All gain medium transitions have an intrinsic linewidth associated with the finite lifetime and spontaneous decay of electrons in the upper state. It can be shown that the intrinsic linewidth $\Delta\nu_{int}$ (FWHM) is related to decay time t_{sp} of the upper state as

$$\Delta\nu_{int} = \frac{1}{2\pi t_{sp}} \tag{2}$$

Nd:YAG, the lasing medium for the lasers tested in this thesis, has a decay time of

$$t_{sp} \approx 215\,\mu s \Rightarrow \Delta\nu_{int} \approx 740\,Hz$$

For most lasers however, the intrinsic linewidth is completely dwarfed by other line-broadening mechanisms, and Nd:YAG is not an exception. The dominant line-broadening mechanism for Nd:YAG is collision broadening, where phonons in the crystal disrupt the interactions between the atoms and the EM-field. The collision linewidth is highly dependent on the lattice temperature of the crystal, but at 300 K the linewidth $\Delta\nu_{col}$ has been measured for Nd:YAG as

$$\Delta\nu_{col}(300\,K) \approx 120\,GHz$$

It should be noted that this linewidth only gives a conservative estimate for the breadth of frequencies that could experience lasing in Nd:YAG around 1064 nm. Firstly, as the laser is continuously pumped it would not be unlikely for it to reach temperatures quite a bit above room temperature (300-350 K), and at 350 K the linewidth is increased by approximately 50% ($\Delta\nu_{col}(350\,K) \approx 180\,GHz$). Secondly, transition linewidth is defined as the full width half maximum (FWHM) of the spectral line gain profile and, depending on the gains and losses in the cavity, light with frequencies beyond the interval set by the linewidth could still potentially overcome the threshold for lasing.

2.2.2 Resonator modes

The transition frequency and linewidth are not the only factors to affect which frequencies are allowed to lase, the design of the oscillation cavity will introduce additional criteria. In order for an EM-field to build up in the cavity it

must reproduce itself after one round trip, or the fields from successive round trips won't add up in phase, resulting in destructive interference. This restricts the oscillating field to consist of discrete field distributions called longitudinal modes. For light traveling on the optical axis the requirement for the mode to exist is that the phase shift after one round trip is a multiple of 2π , assuming a simple two mirror cavity with length L gives us the relation

$$2kL = 2n\pi,\ n = 1,2,3,... \Rightarrow \nu = n(\frac{c}{2L}) \Rightarrow \Delta\nu = \frac{c}{2L} \tag{3}$$

where k is the wavenumber and L is the optical path length.

2.2.3 Competing modes and spatial hole burning

If we consider a simple two mirror cavity with optical path length of 50 mm, equation (3) gives us a mode spacing $\Delta\nu = 3\,GHz$. If this cavity is built around a Nd:YAG crystal with a linewidth of 120 GHz we could potentially fit at least 50 transverse modes inside the gain curve. All of these modes will not usually lase at the same time though. This is because the Nd:YAG linewidth is almost exclusively homogeneously broadened, which is to say that all the ions in the crystal are equally affected by collision broadening and thus are all equally likely to interact with a photon under the line profile. As the modes closest to the center of the line profile experiences the most gain they will begin to lase first and thus should be able to dominate all the interactions with the generated population inversion, stealing most of the gain and preventing modes farther from the transition frequency from experiencing enough gain to lase.

But there is a phenomenon that allows modes farther from the transition frequency to lase, and it is called spatial hole burning. As the EM-field of the strongest mode propagates back and forth inside the cavity a standing wave pattern is generated. This means that throughout the cavity, including inside the gain medium, there will be nodes and antinodes of the EM-field. In the antinodes the field will be largely non-existent, and any population inversion built up will not be able to interact with the main mode. This creates pockets of available gain inside the gain medium that can feed additional modes.

2.3 Methods for single mode selection

A broad linewidth and spatial hole burning presents challenges when one wants to operate a laser on a single longitudinal (SLM) mode but there are techniques one can use to encourage SLM. By introducing optical elements with wavelength dependent losses it is possible to engineer a bandpass filter in the cavity. It can be enough to introduce only small single pass losses to side modes in order to suppress them and leave the laser operating in SLM. Another strategy would be to combat the spatial hole burning. As long as the laser is mostly homogeneously broadened, and no standing wave is built up in the cavity, a single mode should experience the most gain during upstart and once lasing should continue to do so in solitude until the mode is tuned far off the center of the gain curve. We will now look closer at some of the techniques implemented in the lasers of this thesis to facilitate SLM. First we will consider two types of bandpass filters; a Fabry Perot etalon and a Lyot-filter. Then we will look at a strategy to prevent spatial hole burning that is used in the ring cavity lasers; a unidirectional resonator.

2.3.1 Fabry Perot etalon

A FP etalon consists of a transparent plane-parallel plate with both plane sides reflective. As light enters the etalon and is reflected back and forth, the field of transmitted light will be a superposition of the light that travels straight through

without reflection together with all the fields that experience one or more round-trips in the etalon before transmission. For wavelengths where all contributions add up in phase this will result in positive interference and increased transmission, whereas for wavelengths where contributions do not match in phase the result will be destructive interference and reduced transmission. The criteria for repeated reflections to add up in phase is:

$$\nu_{etalon} = \frac{nc}{2D}\,, n = 1,2,3,... \tag{4}$$

where D is the optical path length between the two plane surfaces.

2.3.2 Lyot filter

A Lyot filter consists of a birefringent crystal as well as polarization filters or other polarization selective optical elements. The filter takes advantage of the wavelength dependent phase shift between ordinary and extraordinary components of the propagating beam as it travels through the birefringent crystal. The phase shift between ordinary and extraordinary components after one pass through the crystal is:

$$\Delta\phi = \frac{2\pi}{\lambda}(n_e - n_o)L_{crystal} \tag{5}$$

If the phase shift corresponds to a multiple of 2π the polarization of the beam will remain the same before and after the crystal and the beam will travel unimpeded through the polarization selective elements. However, if the phase shift is not a multiple of 2π the beam will exit the crystal with some form of elliptical polarization and will experience losses at the polarization selective elements. Specifically for the lasers in this thesis, the polarization selective elements consist of mirrors designed with much higher reflection for one of the two polarizations.

The selection rule for which frequencies travel through the Lyot filter without loss is:

$$\nu_{Lyot} = \frac{nc}{(n_e - n_o)L_{crystal}}, n = 1,2,3,... \tag{6}$$

2.3.3 Unidirectional resonator

A unidirectional resonator deals with the issue of spectral hole burning by simply preventing standing wave fields from building up inside the cavity. Since standing wave fields are the result of counterpropagatíng fields inside the cavity all that is required is restrict the field to propagating in only one direction, and that is the purpose of the unidirectional oscillator. This is achieved by introducing a Faraday rotator, a phase plate and polarization selective elements.

The Faraday rotator is a transparent material with a strong magnetic field applied to it, such that the magnetic flux is parallel to the direction of propagation. As light with a linear polarization travels through the transparent material, the polarization will be rotated by an angle that is dependent on the length and composition of the material as well as the strength of the magnetic field. The direction in which the polarization is rotated is only dependent on the direction of the magnetic flux and is not dependent on the direction of beam propagation. This is opposite to how a phase plate operates, where the rotation of polarization is dependent on the direction of propagation. Thus it is possible to design a pair of rotator and phase plate such that beam propagating in one direction will have its polarization rotated a small amount in the rotator and then have the contribution from the phase plate cancel that rotation. Naturally, if the beam is propagating in the opposite direction the phase plate will instead add to the polarization change of the rotator and the beam will experience losses at the polarization selective elements in the cavity.

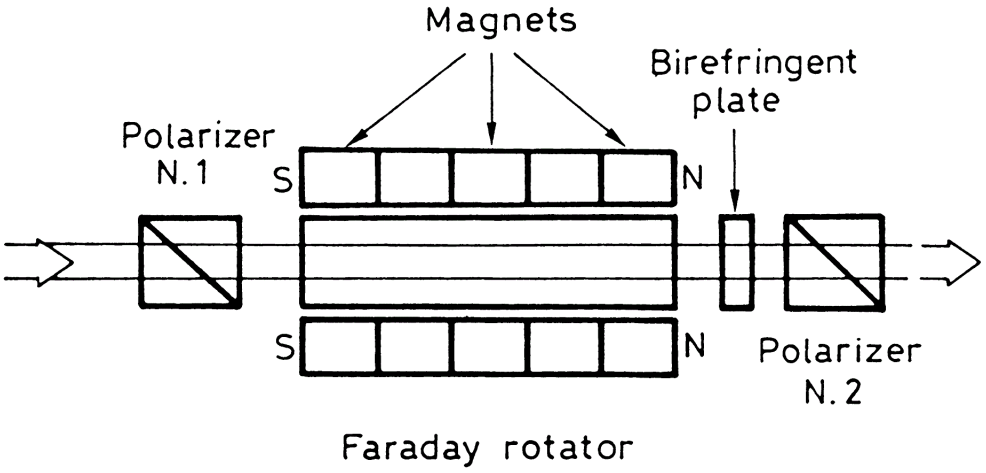

Figure 1: Unidirectional device using a Faraday rotator (optical-diode), *Orazio Svelto, Principles of Lasers 4th Ed.*

2.4 Non-linear optics

2.4.1 Non-linear polarization in optical materials

Usually when we allow light to propagate through some medium we will induce a polarization within the material that is linear with respect to the propagating electric field. The polarization can be expressed as:

$$P = \varepsilon_0 \chi E \tag{7}$$

where χ is the linear susceptibility of the material. From χ we can determine both the refractive index and the absorption in the material as light propagates through it.

But the linear response of the material to an applied electric field is only an approximation and like many linearizations it only holds true under certain conditions. As long as the electric field is not too strong, the approximation holds up well. But when dealing with intense EM fields such as those that exist inside focused powerful laser beams the polarization response reveals itself to be nonlinear and should actually be expressed as:

$$P = \varepsilon_0(\chi^{(1)}E + \chi^{(2)}E^2 + \chi^{(3)}E^3 + ...) \tag{8}$$

Where $\chi^{(1)}$is the linear susceptibility and $\chi^{(2)}, \chi^{(3)}, ...$ are the non-linear susceptibilities.

The non-linear polarization terms are all responsible for a range of processes and phenomena in optics but in this thesis we will only concern ourselves with the first nonlinear term; the quadratic polarization

$$P^{(2)} = \varepsilon_0 \chi^{(2)} E^2 \tag{9}$$

This is the term responsible for the second harmonic generation that is used in Cobolt lasers to frequency double the light inside the cavity before output.

2.4.2 Second harmonic generation

The quadratic polarization $P^{(2)} = \varepsilon_0 \chi^{(2)} E_1 E_2$ allows two fields E_1 and E_2 with frequency ω_1 and ω_2 to interact and induce a polarization that in turn generates a field E_3 with frequency $\omega_3 = \omega_1 + \omega_2$

This is known as sum frequency generation, and if we assume that the two fields interacting have the same frequency ($\omega_1 = \omega_2 = \omega, \omega_3 = 2\omega$) we arrive at the process of second harmonic generation, which allows us to focus a beam with frequency into a medium with quadratic susceptibility and generate light with frequency 2ω.

It can be shown that, assuming SVEA[1], the two field at ω and 2ω in the non-linear crystal, propagating in x-direction can be described by coupled wave equations as follows:

$$\frac{\partial E_\omega}{\partial x} = \frac{i\omega}{n_\omega c} d_{eff} E_{2\omega} E_\omega^* exp[ix(k_{2\omega} - 2k_\omega)] \tag{10}$$

$$\frac{\partial E_{2\omega}}{\partial x} = \frac{i\omega}{n_{2\omega} c} d_{eff} E_\omega E_\omega exp[-ix(k_{2\omega} - 2k_\omega)] \tag{11}$$

n_i is the refractive index, k_i is the wavenumber and d_{eff} is the effective nonlinear coefficient

Integrating the lower equation over crystal length L, and expressing the intensity of the wave as

$$I_{2\omega} = \frac{1}{2} \varepsilon_0 c n_{2\omega} |E|^2 \tag{12}$$

Gives the intensity of field at frequency 2ω after a crystal of length L as:

$$I_{2\omega} = \frac{2\omega^2 d_{eff}^2 L^2 I_\omega^2}{n_{2\omega} n_\omega^2 \varepsilon_0 c^3} sinc^2(\frac{\Delta k L}{2}) \tag{13}$$

where $\Delta k = k_{2\omega} - 2k_\omega$, and $sinc(x) = \frac{sin(x)}{x}$

2.4.3 Phase matching

Δk is called the phase-mismatch for the second harmonic generation and as can be seen from the expression for intensity above, if it has a constant non-zero value the intensity of the generated beam will only ever oscillate between zero and some positive value as we vary the length of the crystal. On the other hand, if $\Delta k = 0, sinc(0) = 1$, and the intensity of the field at frequency 2ω will increase quadratically with the length of the crystal. There are techniques to minimize the phase-mismatch but assuming a non-zero Δk we can only make the crystal a certain length before extra material only causes energy to flow back to the original field at frequency ω. We can calculate the length of crystal that gives maximum generation of the second harmonic.

$$[x^2 sinc^2(x)]_{max} = (\pm\frac{\pi}{2})^2 sinc^2(\pm\frac{\pi}{2}) \Rightarrow \frac{|\Delta k| L_{max}}{2} = \frac{\pi}{2} \Rightarrow L_{max} = \left|\frac{\pi}{\Delta k}\right| \tag{14}$$

L_{max} is referred to as the coherence length.

[1] Slowly-Varying Envelope Approximation, see Appendix A for further details.

2.4.4 Quasi phase matching

While it is possible to achieve zero phase-mismatch, for instance by taking advantage of the birefringence in the non-linear crystal there are often drawbacks that limit the feasibility of such solutions. A different approach to improving the SHG is to circumvent the limitation set by coherence length by using a crystal longer than the coherence length but periodically varying the structure of the crystal to counteract the phase-mismatch, and this is referred to as quasi phase matching.

A simple example of quasi phase matching would be if we took a nonlinear crystal of length $2L_{max}$, cut it in half and rotated the second half by 180°. Cutting and rotating crystal wafers is not usually the most practical way of achieving quasi phase matching though and the lasers in this thesis utilize a far more convenient method to create periodic structures in nonlinear crystals, called periodic poling. Periodic poling works by depositing periodic electrodes on the non-linear crystal and using those electrodes to apply a strong electric field. This causes periodic sign reversal of the effective nonlinear coefficient d_{eff} in the crystal which counteracts the sign reversal caused by the phase-mismatch.

2.5 Theoretical calculations

2.5.1 Approximate mode spacings

A rough estimate of the mode spacing for the lasers tested in this thesis can be calculated by determining the length of the cavity as well as thickness of the larger optical elements in the optical path. For the standing wave lasers the formula used was: $\Delta\nu = \frac{c}{2L}$ where L is the optical path length between the two mirrors. For the ring cavity the formula is $\Delta\nu = \frac{c}{L_p}$ where L_p is the optical path length of the closed path around the ring cavity. Note that the spacing between modes calculated is before second harmonic generation. See section 3.1 for more details on the lasers.

532-1/532-M/532-C lasers:

These three variations of a 532 nm standing wave laser share roughly the same amount of optical elements as well as size of oscillation cavity. The length of the cavity is approximately 35 mm, and contains a number of optical elements with higher refractive index($n \approx 2$). Taking into account the added optical path length from these optical elements we arrive at an estimate for the optical path length and longitudinal mode spacing:

$$L = 45\,mm \Rightarrow \Delta\nu = \ 3.3\,GHz \tag{15}$$

561-1 laser:

The 561-1 laser has a slightly shorter cavity length at approximately 25 mm, and contains a number of optical elements with higher refractive index($n \approx 2$): Taking into account the contribution of these elements we arrive at an estimate for the longitudinal mode spacing:

$$L = 33\,mm \Rightarrow \Delta\nu = \ 4.5\,GHz \tag{16}$$

532-R/561-R lasers:

The 532 nm and 561 nm ring cavity lasers have approximately the same ring cavity length and optical elements. The length of the ring cavity is approximately 70 mm and contains a number of optical elements with higher refractive index($n \approx 2$). Taking into account the additional optical path length from these components we arrive at:

$$L_p = 91.5\,mm \Rightarrow \Delta\nu = \ 3,3\,GHz$$

2.5.2 Lyot filter FSR

Using equation (6) we can determine the spacing between frequencies that experience minimal losses in the Lyot filter, the free spectral range of the Lyot filter.

$$\Delta\nu_{Lyot} = \frac{c}{L(n_e - n_o)} \tag{17}$$

The Lyot filter material for this thesis is KTP, which is biaxial with Sellmeier equations

$$n_x^2 = 3.291 + \frac{0.04140}{(\lambda^2 - 0.03978)} + \frac{9.35522}{(\lambda^2 - 31.45571)} \tag{18}$$

$$n_y^2 = 3.45018 + \frac{0.04341}{(\lambda^2 - 0.04597)} + \frac{16.98825}{(\lambda^2 - 39.43799)} \tag{19}$$

$$n_z^2 = 4.59423 + \frac{0.06206}{(\lambda^2 - 0.04763)} + \frac{110.80672}{(\lambda^2 - 86.12171)} \tag{20}$$

If we know these refractive indexes and the angles of propagation through the crystal we can determine n_e and n_o for the Lyot filter.

$$n_o = [Acos^2\rho + Bsin^2\rho + 2Csin(\rho)cos(\rho)]^{\frac{-1}{2}} \tag{21}$$

$$n_e = [Asin^2\rho + Bcos^2\rho + 2Csin(\rho)cos(\rho)]^{\frac{-1}{2}} \tag{22}$$

$$A = \frac{cos^2\theta cos^2\phi}{n_x^2} + \frac{cos^2\theta sin^2\phi}{n_y^2} + \frac{sin^2\theta}{n_z^2} \tag{23}$$

$$B = \frac{sin^2\phi}{n_x^2} + \frac{cos^2\phi}{n_y^2} \tag{24}$$

$$C = (\frac{1}{n_y^2} - \frac{1}{n_x^2})cos(\theta)sin(\phi)cos(\phi) \tag{25}$$

$$\rho = \frac{1}{2}tan^{-1}(\frac{2C}{A-B}) \tag{26}$$

Given values for the parameters $(\lambda, \phi, \theta, L)$ of the Lyot filter used in this thesis, it can be determined that the FSR for the filter is:

$\Delta\nu_{Lyot} \approx 590\,GHz$

The FSR of the Lyot filter is quite a bit larger than the linewidth for the Nd:YAG at 1064 nm (~120-180 GHz) and we should not need to worry about multiple bands of transmission being under the gain curve simultaneously.

2.5.3 Fabry Perot etalon FSR

Using equation (4) we can determine the free spectral range of the etalon, the spacing between transmitted frequencies, as

$$\Delta\nu = \frac{c}{2nd} \tag{27}$$

where n is the refractive index and d is the thickness of the etalon.

The etalons used in the lasers of this thesis measure a variety of thicknesses and the FSR can be determined range over:

$200\,GHz < \Delta\nu_{FP} < 1000\,GHz$

This means that the thickest etalons will have FSRs comparable to the spectral width estimated for the gain profile of Nd:YAG at 1064 nm (~120-180 GHz). Using single thick etalon there is a risk of fitting two separate transmission bands under the gain curve of the laser, and thus additional bandpass filters could be required to ensure SLM operation.

3 Equipment and Methodology

3.1 Diode pumped solid state lasers

The majority of measurements were performed on four models of lasers; two standing wave laser models and two ring cavity models:

532 nm standing wave laser (532-1):

The 532-1 series has a laser diode emitting 808 nm light, which is used to pump a Nd:YAG crystal. This causes the Nd:YAG crystal to emit stimulated emission at 1064 nm, and this light is then frequency doubled to 532 nm by allowing the beam to pass through a PPKTP crystal. The cavity for the oscillating 1064 nm light consists of two end mirrors, resulting in a standing wave pattern inside the cavity. In addition to the laser medium, mirrors and PPKTP most 532-1 lasers also include bandpass filters to facilitate SLM operation.

561 nm standing wave laser (561-1):

The 561-1 series, same as the 532-1, uses a Nd:YAG crystal pumped with 808 nm light, but the laser utilizes a different transition and is made to oscillate at 1123 nm rather than 1064 nm. The transition associated with 1123 nm is one of the weaker for Nd:YAG and requires that the stronger transitions such as 1064 nm, 1319 nm and 946 nm to be blocked, in order to experience enough gain for lasing. Once generated, the 1123 nm light is passed through a PPKTP for frequency doubling into 561 nm. The 561-1 contains several bandpass filters to encourage SLM.

532 nm unidirectional ring cavity laser (532-R):

The 532-R series emits laser light at 532 nm and the light is generated by the same mechanisms as the 532-1 series (Pumping at 808 nm, frequency doubling 1064 nm light into 532 nm light). The difference is that the 532-R series of lasers are built in a configuration that allows unidirectional oscillation in a ring cavity and no standing wave electromagnetic field.

561 nm unidirectional ring cavity laser (561-R):

The 561-R series emits laser light at 561 nm, by the same type of frequency mixing as for the 561-1 series, but the cavity is designed as a unidirectional ring oscillator without a standing wave EM-field.

Additionally, a small amount of lasers of three other models of lasers were tested; a single modified 532 nm standing wave laser, two compact 532 nm lasers and a single modified 1064 nm laser:

Modified 532 nm standing wave laser (532-M) :

The prototype 532-M is very similar to 532-1 lasers in term of cavity design but uses a modified packaging of the cavity.

532 nm standing wave laser with compact packaging(532-C):

The 532-C is a more compact version of the 532-1 but the cavity length and optical components remain the same.

Modified 1064 nm unidirectional ring cavity laser(1064-M):

The prototype 1064-M is built as a ring laser emitting 1064 nm, achieved by pumping a Nd:YAG crystal and simply outcoupling some of the power built up in the cavity. Thus no frequency mixing is required. The most interesting aspect of the 1064-M, from a testing perspective, is that while the cavity is designed similarly to the other ring lasers (532-R, 561-R), the design of the packaging, internal base plate and TEC placement is more similar to that used for the 532-1 and 561-1 models. This should allow us to test how the ring cavity design performs with similar packaging to that of the standing wave lasers.

3.2 Fabry Perot interferometer

The Fabry Perot interferometer used was a SA210-5B from Thorlabs. The SA210 is a confocal scanning FPI, consisting of two confocal mirrors, a piezoelectric transducer to adjust the spacing of the mirrors, and a photodiode to detect the intensity of the transmitted light. The free spectral range of the SA210 is 10 GHz, with a finesse of at least 150. The reflective coating on the mirrors is designed for an operation range from 534 nm to 820 nm. A control box (SA201) is attached to the SA210 to supply the ramp signal to the piezoelectric transducer and to amplify the signal from the photodetector.

3.3 Oscilloscope

The amplified signal of the FPI photodiode was observed using a Tektronix oscilloscope model DPO 2024. A trigger signal from the SA201 was used for oscilloscope triggering. The time scale of the oscilloscope window was adjusted so that a single signal peak from the FPI was traced at both ends of the oscilloscope window, resulting in the oscilloscope window spanning a frequency interval of one free spectral range for the FPI, 10 GHz. The oscilloscope allowed waveform data of the trace to be extracted using a USB connection, see figure 2 for an example of oscilloscope waveform data.

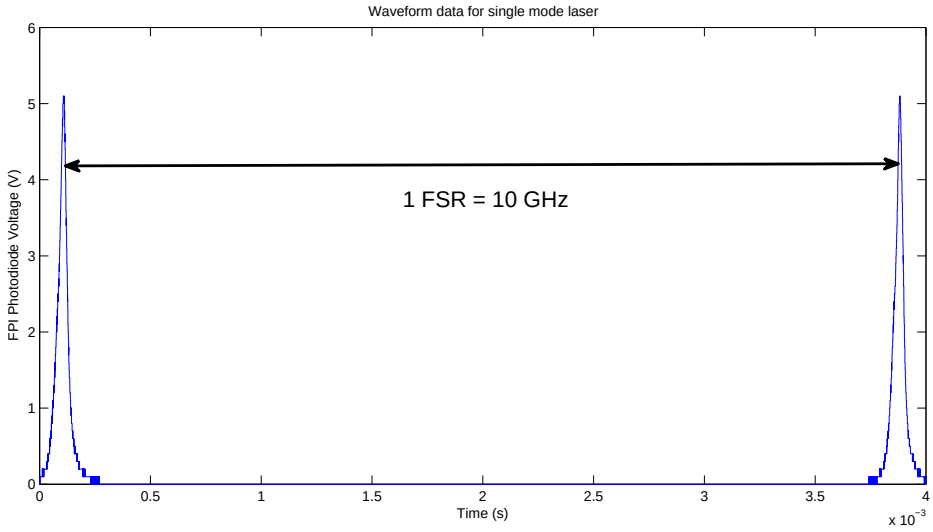

Figure 2: Plot of waveform data from the oscilloscope for a SLM operating laser

3.4 Wavemeter

The wavemeter used for the measurements was a Wavemaster from Coherent Inc. The equipment consists of a sensor head with built in beam splitter, a fiber optic cable, and the Wavemaster itself. The measuring principle of the WM is based on measurements of high order diffraction patterns. The WM displays frequency values with a resolution of 0.1 GHz. A measurement was set up during work on this thesis to test the resolution of the WM. A laser operating on SLM was tuned over a small range of frequencies ($\sim$3 GHz) and changes in frequency were measured using the WM and oscilloscope. See figure 3 for plot of results for this test. The results suggest that the WM agrees with the FPI up to an error of $\pm 0.1\,GHz$ when tuning over 3 GHz during a short period.

The Wavemeter has a built-in automatic calibration function which periodically references neon spectral lines in order to re-calibrate and maintain accuracy.

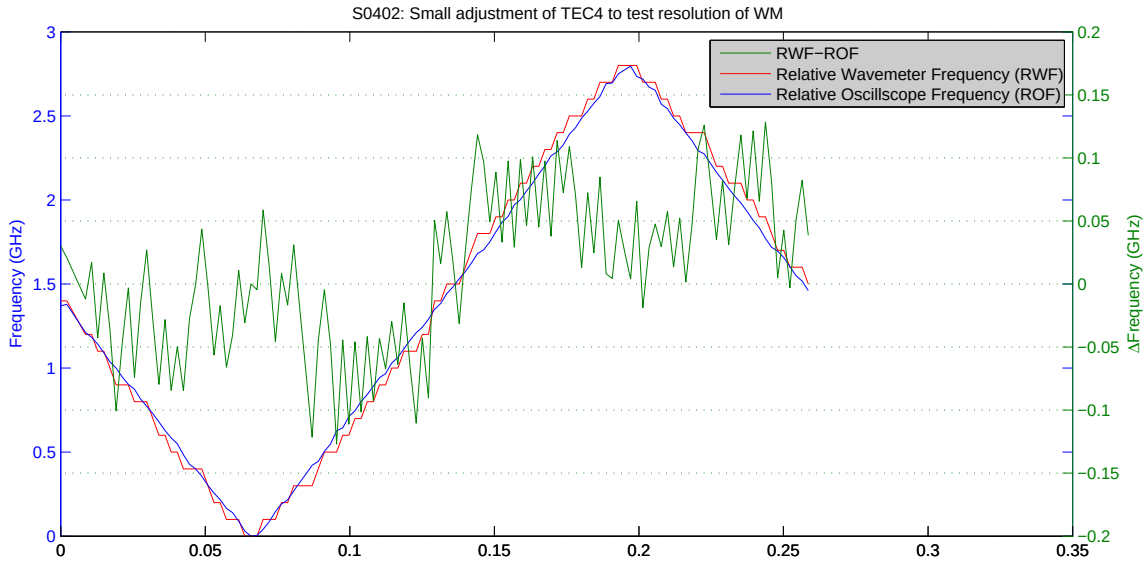

Figure 3: Test of Wavemeter resolution by continuous tuning of laser frequency

3.5 Temperature controlling Peltier elements (TECs)

The temperature of the base plate on which the laser was placed during testing was controlled using a Peltier element, sometimes referred to as a thermoelectric cooler (TEC). A Peltier element allows the user to induce and control heat flow across the element by applying and varying voltage to the device. Smaller TECs are also located in some sections of the lasers, in order to control the temperature at optical elements such as the diode laser, the Lyot-filter or the internal plate on which the optical elements are attached.

3.6 FPI peak detection and logging of measurement data

A Labview program was written to control base plate/internal TECs while logging data from the laser, baseplate, wavemeter and FPI. Labview's built-in waveform peak detection function (*Waveform Peak Detection VI*) was used to analyze the FPI waveform data relayed from the oscilloscope.

3.7 Lab setup

In order to avoid saturating or damaging the FPI or WM, a beamsplitter was used to divert approximately 90% of the radiation before directing the remainder into the measuring equipment. Placement of the wave meter sensor head varied, either being placed before or after the beam splitter, in order to achieve appropriate intensity of incoming light to the WM. The focusing lens had a focal length = 15 cm, and was placed such that the middle of the FPI cavity was positioned in the focus of the lens. Additional absorptive filters were sometimes included to further reduce intensity of light entering the WM and FPI.

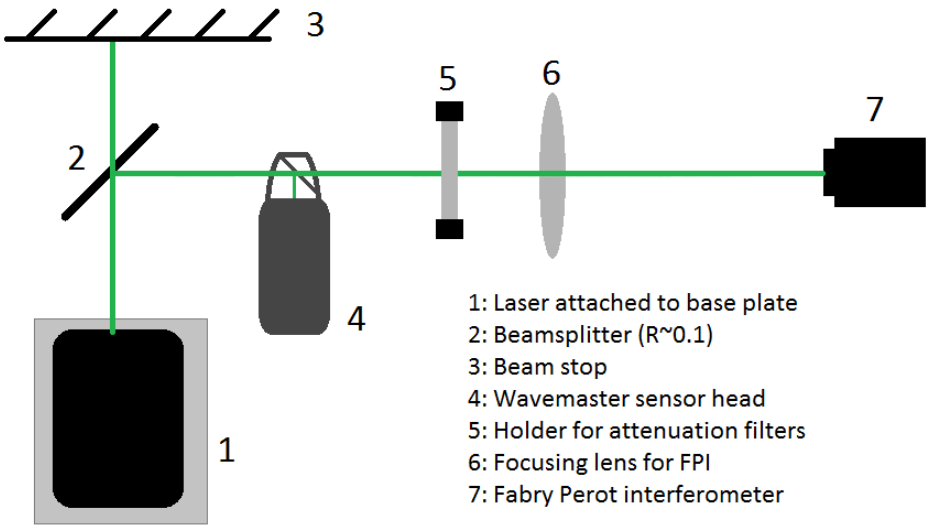

Figure 4: Illustration of Setup

3.8 Baseplate temperature cycling methodology

The laser was attached to the baseplate and turned on. The position of the beamsplitter was adjusted so as to direct the beam through the center of the focusing lens for the FPI. The position of the FPI was then adjusted until a sharp peak was visible on the oscilloscope. The sensor head of the WM was placed in the beam directly before or after the main beamsplitter so that a small amount of light could be sampled by the WM beamsplitter without having a significant impact on the FPI signal. Once the oscilloscope, wavemeter and drivers for baseplate and laser were connected to a PC, the test program was executed. The temperature of the baseplate started at $35\,^{o}C$ and was adjusted according to a time-dependent sinusoidal profile with an amplitude of $15\,^{o}C$, and a period of 4 hours. Each laser went through two such periods for a total measurement time of 8 hours.

For the baseplate temperature cycling measurements a time delay of 10 seconds was included between changing the setting for the baseplate TEC temperature and logging the measurement values, in order to give the TEC controller sufficient time to reach the correct temperature and stabilize.

3.9 Stationary baseplate temperature methodology

The measurement at constant baseplate temperature was performed directly after the completion of the temperature cycling, to take advantage of the already completed setup. The same delay of 10 seconds was used for the measurement, and a total measurement time of 8 hours was used. Additionally a few longer tests with durations of several days were performed.

3.10 Internal TEC temperature cycling methodology

The internal TEC measurements were performed using the same setup as the baseplate temperature cycling measurements but was performed over a shorter time period, and with adjustments to laser TEC temperature settings rather than base plate settings. The measurement was divided into several sequences and during each sequence one TEC was varied over an interval of temperatures centered on the TEC temperature value set by production, while the other TECs were held at constant temperature. The delay between updating TEC temperature setting and logging measurements was lowered to 2 seconds as internal TECs were smaller and thus stabilized in less time. Temperatures of the TECs were varied by a constant step value of $0.05\,^oC$, with an amplitude of either 2 or $4\,^oC$.

4 Results

4.1 Base plate temperature cycling

Two log files are created with each base plate temperature cycling measurement, organized as follows:

- **Temperature cycle measurement log (TCM):** Time, Base plate temperature, Number of detected peaks, FPI frequency for largest peak, FPI amplitude for largest peak, temperature of internal TECs, WM frequency
- **Multi-peak Log (MP):** Time, Base plate temperature, FPI peak frequencies, FPI peak amplitudes

The TCM log contains data for every step in the measurement, whereas the MP log only stores information about peaks when the peak detection function returns #Peaks > 1. Based on the TCM data, it is possible to determine for which base plate temperatures the laser is operating on a single longitudinal mode as well as how the frequency of the strongest laser mode varies with temperature both continuously and in distinct mode jumps. The MP log gives information about the side modes when they appear on the FPI, such as how strong they are and how they are positioned relative to the main mode. FPI peak frequency takes a value between 0 and 10 GHz depending on what part of the oscilloscope trace the peak is detected, and one should note that changes in peak position only represents the real change in frequency as long as the new peak frequency remains within the same free spectral range as the previous peak measurement. If a mode jump of 7 GHz takes place this can manifest as a mode jump of 7 GHz or -3 GHz on the FPI as the FSR is only 10 GHz.

4.1.1 Defining ROF & RWF

Since we are only concerned with how the frequency changes during testing, not the absolute value of frequency, we introduce two variables RWF (Relative Wavemeter Frequency) and ROF (Relative Oscilloscope Frequency). These variables are defined as

$RWF_i = \nu_{i,WM} - \nu_{min,WM}$

$ROF_i = \nu_{i,Osc} - \nu_{min,Osc}$

where $\nu_{i,WM}$ is the frequency value from the WM for data point i, $\nu_{min,WM}$ is the minimal frequency value from the WM for the entire measurement, $\nu_{i,Osc}$ is the frequency value of the oscilloscope (based on peak detection of oscilloscope data) for data point i and $\nu_{min,Osc}$ is the minimal frequency value from the oscilloscope for the entire measurement.

4.1.2 Plots of changes in frequency based on FPI and WM data

The two variables ROF & RWF can be plotted together with base plate temperature against time to illustrate what happens to the frequency of the largest mode during temperature cycling. Examples of such plots can be seen for measurements on a 532-1, a 561-1, a 532-R and lastly a 561-R in figures 5, 6, 7 and 8.

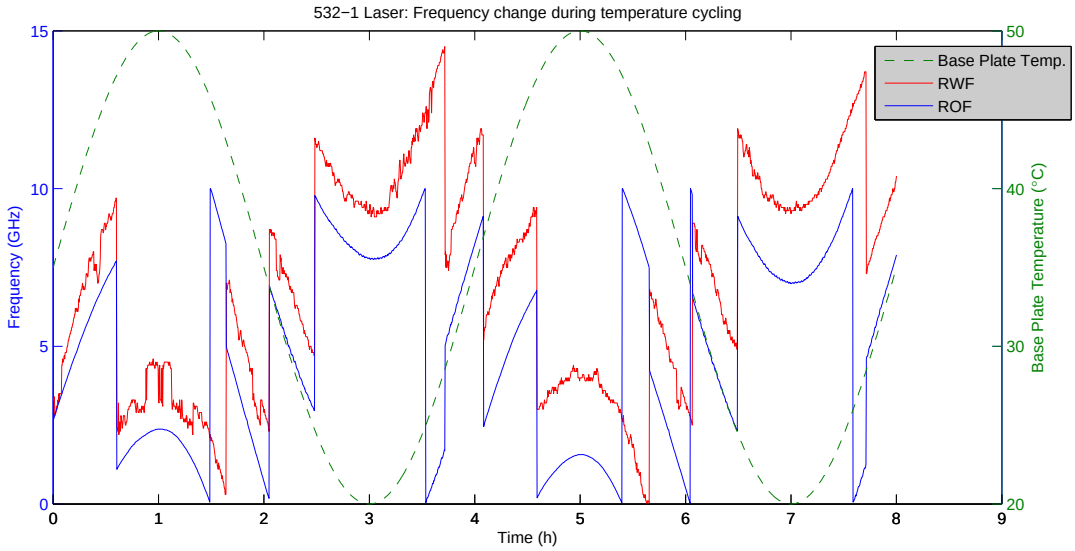

Figure 5: Plot of frequency change for 532-1 laser during temperature cycling (ID#:3)

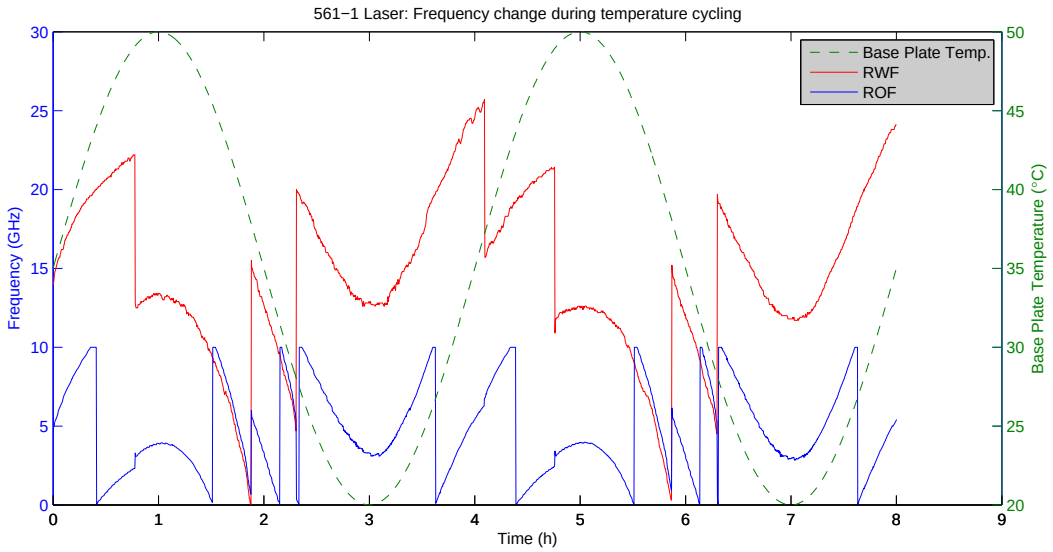

Figure 6: Plot of frequency change for 561-1 laser during temperature cycling (ID#:17)

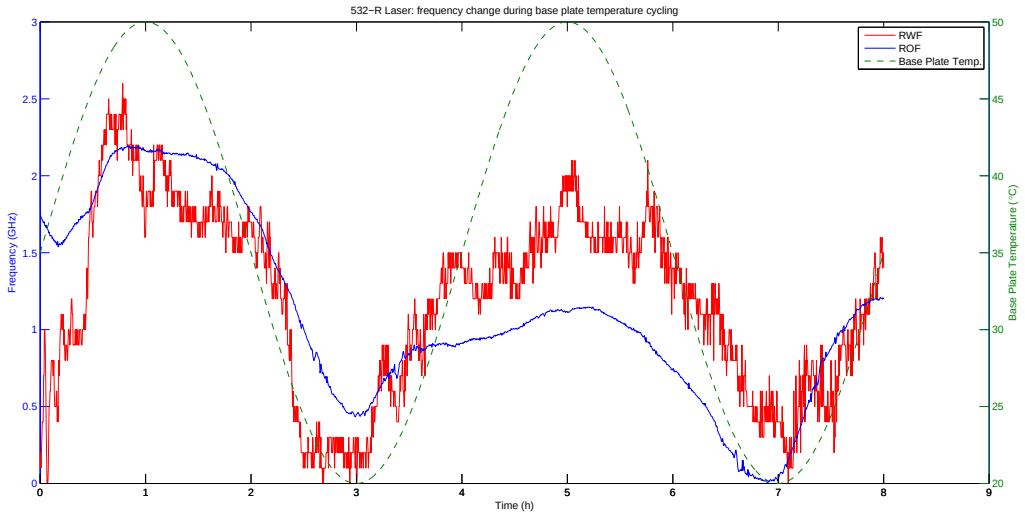

Figure 7: Plot of frequency change for 532-R laser during base plate temperature cycling (ID#:R5)

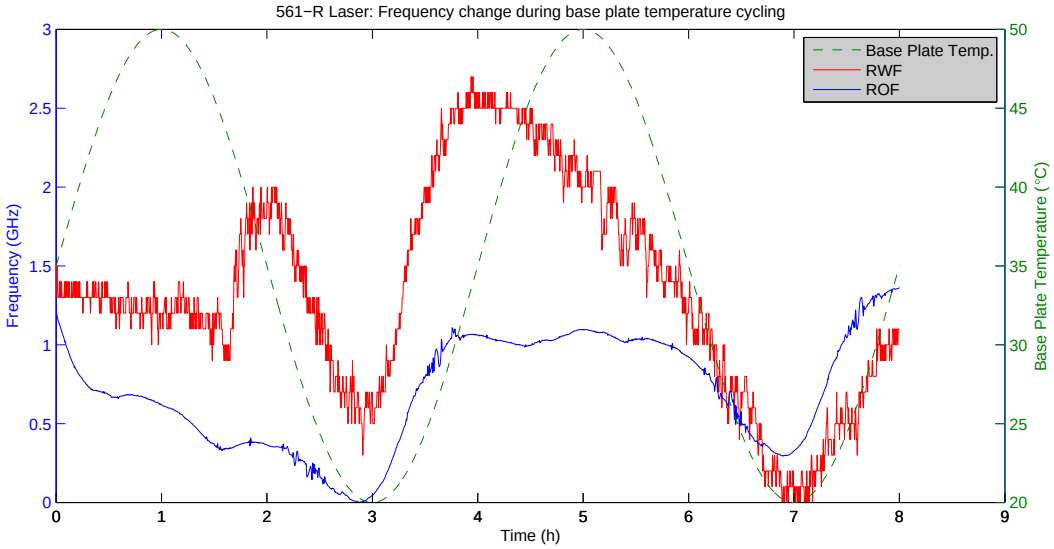

Figure 8: Plot of frequency change for 561-R laser during base plate temperature cycling (ID#:R7)

4.1.3 Estimating $\Delta\nu/\Delta T_{Base}$ at $T_{Base} = 35\,^{\circ}C$

For each data point a differential was estimated using a simple two point estimation, with $(\nu_i - \nu_{i-1})$ based on FPI peak data,

$[\frac{d\nu}{dT}]_i = \frac{(\nu_i - \nu_{i-1})}{(T_i - T_{i-1})}$

Data points between 34 and 36 °C were then average over, with outliers excluded, to arrive at the final estimate for $\Delta\nu/\Delta T_{Base}$.

4.1.4 Tabulation of temperature cycle measurement results

From the two log files generated for each base plate temperature cycling measurement, a number of characteristic values are extracted for tabulation:

ID#	Identification number for laser (ring cavity lasers begin ID# with R)
ROF_{max}	The highest value of ROF during the measurement; can indicate the span of frequencies measured by the FPI, but is limited to frequency spans $\leq$10 GHz.
RWF_{max}	The highest value of RWF during the measurement; indicating the span of frequencies measured by the WM.
# Jumps/Cycle	A mean of the number of jumps per temperature cycle.[2]
Mean Jump Size	Large, discrete changes in frequency measured by WM are identified as mode jumps; the mean of the size of these jumps are then calculated.
$\Delta\nu/\Delta T_{Base}$@ $35^{\circ}C$	Estimated derivative $\Delta\nu/\Delta T_{Base}$ around the central base plate temperature, $35^{\circ}C$. See section 4.1.3 for details.
Multimode %	Fraction of data points where detected peaks > 1. indicates how often the FPI registers multimode operation in the laser during temperature cycle.

Model	ID #	P (mW)	ROF_{max} (GHz)	RWF_{max} (GHz)	# Jumps / Cyc	Mean Jump Size (GHz)	$\Delta\nu/\Delta T_{Base}$@ 35°C $(GHz/^{\circ}C)$	Multimode %
532-1	1	50	10	12.6	6	6.6	0.53	0
532-1	2	50	10	14.6	6	6.9	0.42	0
532-1	3	50	10	14.5	5.5	6.7	0.48	0
532-1	4	300	10	29.3	8	6.3	1.00	0
532-1	5	50	10	15.5	5.5	6.9	0.49	0
532-1	6	100	10	22	6	7.0	0.50	0
532-1	7	100	10	16.1	4.5	6.9	0.40	5.1
532-1	8	50	10	33.8	12	6.4	0.34	0
532-1	9	100	10	17	6	6.7	0.57	2.7
532-1	10	300	10	18.8	5	4.8	0.46	0
532-1	11	100	10	21.3	6	7	0.40	0
532-1	12	100	10	19.9	8	7.1	0.56	0.6
532-1	13	100	10	17.1	6	7	0.59	0
532-1	14	50	10	14.3	4	7	0.45	0
532-1	15	50	10	25.9	10	6.5	0.47	0
561-1	16	100	10	26.9	5	13.5 up; -11.0 down[a]	0.99	0
561-1	17	150	10	25.7	3.5	15 up. -10 down[a]	0.60	0
561-1	18	150	10	31.8	4	22.4 up; -20.7 down[a]	0.78	0
561-1	19	100	10	24.5	4	16 up; -10 down[a]	0.75	0
561-1	20	50	10	25.0	4	14.8 up; -10.8 down[a]	0.73	0
561-1	21	100	10	27.3	5	11.9 up;-9.3 down[a]	0.70	0
532-C	22	100	10	20.3	6	6.3	0.15	10
532-C	23	150	10	19.7	6	6.7	0.24	1
532-M	24	50	2.5	2.4	0	N/A	0.05	0

Table 1: Base plate temperature cycling results for standing wave lasers

[a]Some 561-1 lasers experienced distinctly different mode jumps sizes when jumping up (to higher frequency) and jumping down (to lower frequency). For this reason two separate means are calculated for these lasers.

Model	ID #	P (mW)	ROF_{max} (GHz)	RWF_{max} (GHz)	# Jumps / Cyc	Mean Jump Size (GHz)	$\Delta\nu/\Delta T_{Base}$@ 35°C $(GHz/^{\circ}C)$	Multimode %
532-R	R1	1000	0.6	1.6	0	N/A	-0.01	0
532-R	R2	500	3.6	2.5	0	N/A	0.08	0
532-R	R3	1500	2.5	2.2	0	N/A	-0.05	0
532-R	R4	1500	2.5	2.0	0	N/A	0.04	0
532-R	R5	1500	2.2	2.4	0	N/A	0.01	0
561-R	R6	500	3.1	2.6	0	N/A	0.04	0
561-R	R7	500	1.4	2.5	0	N/A	0.02	0
561-R	R8	200	3.5	2.6	0	N/A	0.04	0
1064-M	R9	400	7.0	6.1	8	4.1	0.51	0

Table 2: Base plate temperature cycling results for ring cavity lasers

4.1.5 Investigation of multimode measurements

Using the MP log data it is possible to determine when side modes appear for the measurements that registered multimode on the FPI, where on the oscilloscope the peaks were positioned and how large the side modes are compared to the main peak. Four lasers exhibit momentary multimode operation, three 532-1 lasers and two 532-C lasers: #7, #9, #12, #22 and #23. To illustrate the location of the main mode, ROF data from the TCM log is plotted against time. MP log data is then drawn as colored circles over the line plot of ROF data; with x position corresponding to the time when the multiple peaks were detected, y position corresponding to the location on the oscilloscope where the side & main peaks were detected, and color of the circle corresponding to the amplitude of the peak being detected.

532-1 laser #7

Laser #7 exhibited momentary multimode operation, and each time it returned to SLM operation it did so due to a mode jump. The longest period of multimode operation took place at $T = 5\,h$ when the FPI peak detection logged 3 peaks continuously for a 20 minute period before the laser experienced a mode jump. See figure 9 for a plot of multimode locations and amplitudes during base plate temperature cycling of laser #7.

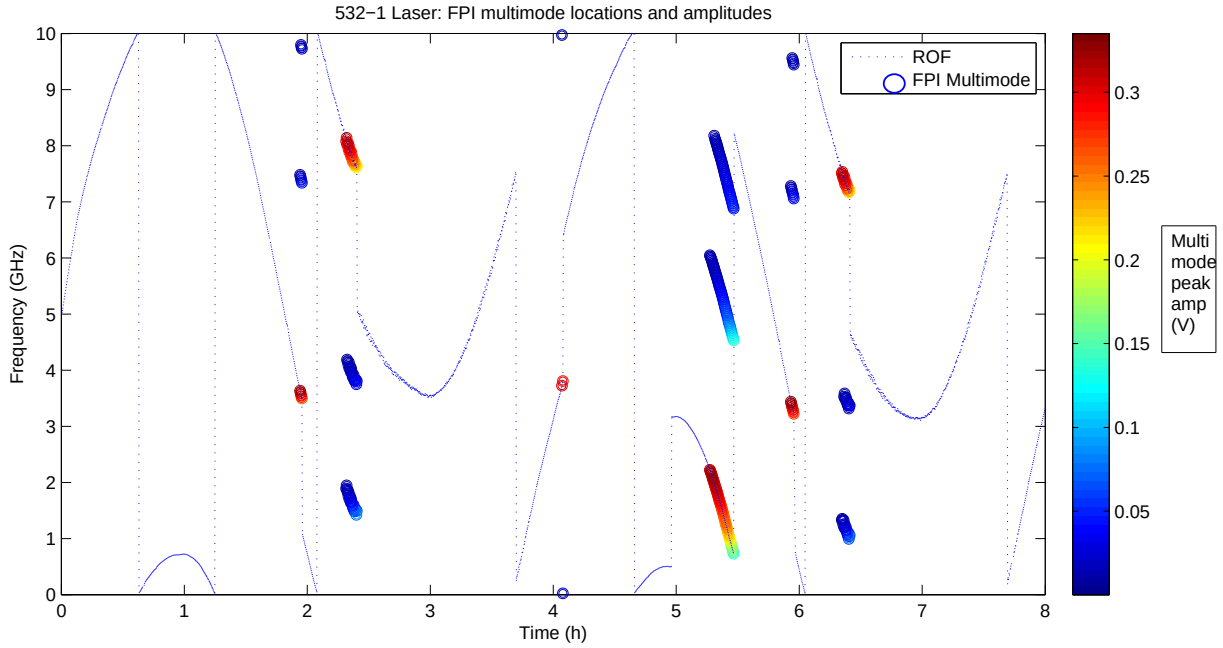

Figure 9: Multimode locations and amplitudes for 532-1 laser (ID#:7)

532-1 laser #9

Laser #9 exhibited multimode operation close to some of its mode jumps but also momentarily entered multimode operation without mode jumping, at T= ~0.3 h and T= ~4h. See figure 10 for a plot of multimode locations and amplitudes during base plate temperature cycling of #9.

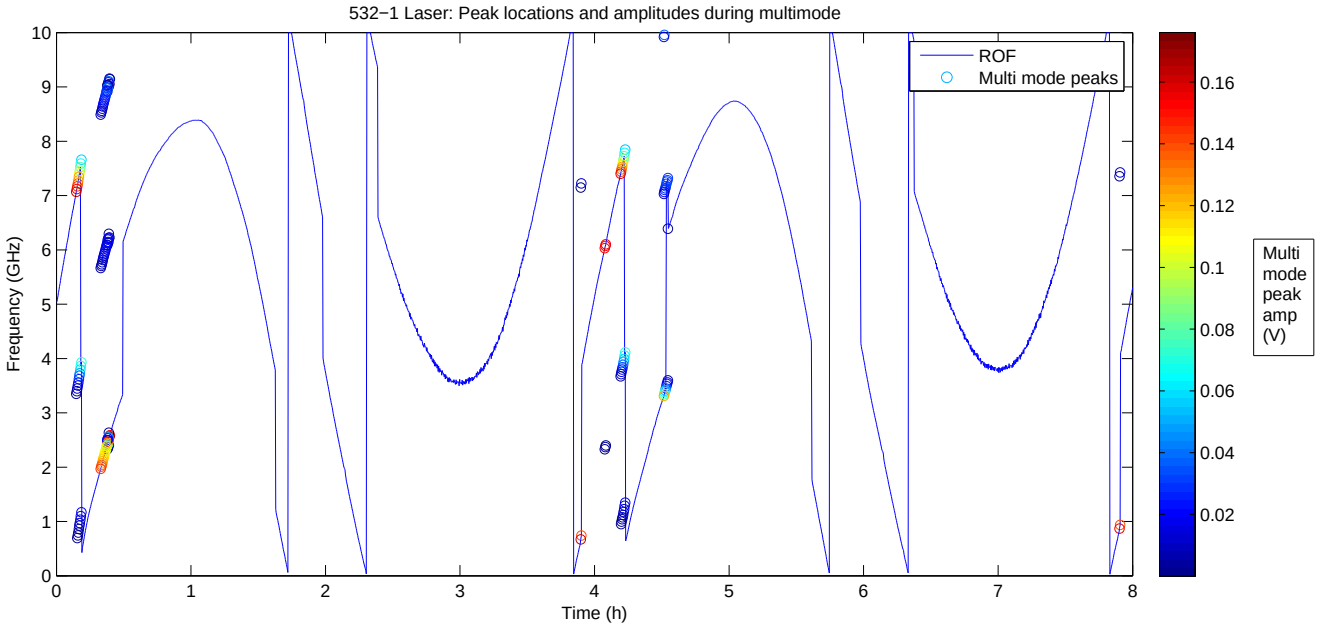

Figure 10: Multimode locations and amplitudes for 532-1 laser (ID#:9)

532-1 laser #12

Laser #12 exhibited weak side modes right before mode jumps.

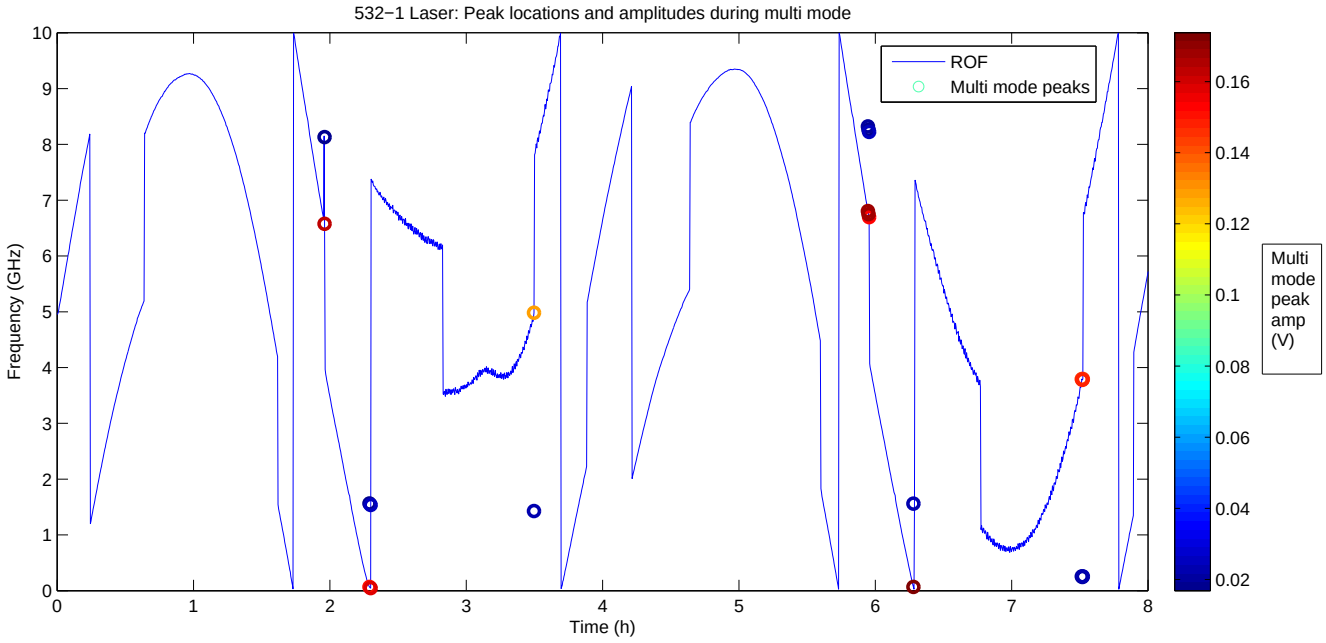

Figure 11: Multimode locations and amplitudes for 532-1 laser (ID#:12)

532-C laser #22

Laser #22 was measured early on in the thesis before the multi-peak log was implemented so we can not see where on the oscilloscope the side modes are located or what their amplitudes are. The FPI amplitude of the main peak was logged though, and by plotting it together with locations of multi-peak detections we can observe that the amplitude of the main peak is not heavily impacted by the existence of additional modes, suggesting that the side modes were quite weak. See figure 12 for a plot of multimode locations as well as amplitude of the main peak during base plate temperature cycling of #22.

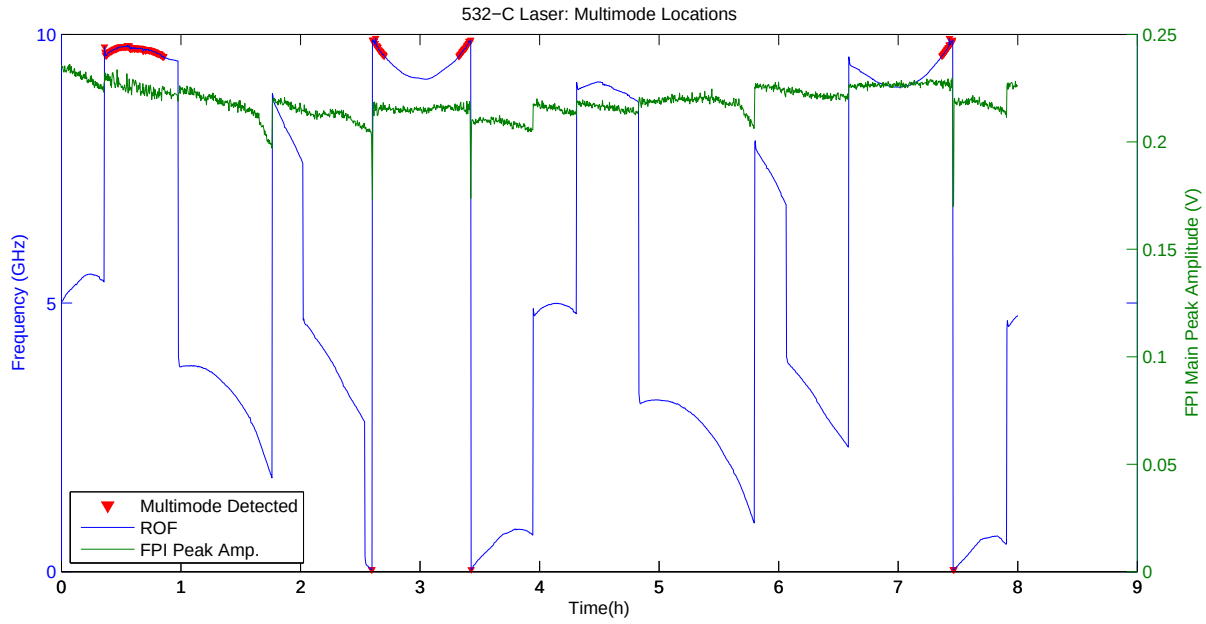

Figure 12: Multimode locations and amplitude of the main peak for S04DPL laser (S/N:6623)

532-C laser #23

Laser #23 exhibited weak side modes right before mode jumps.

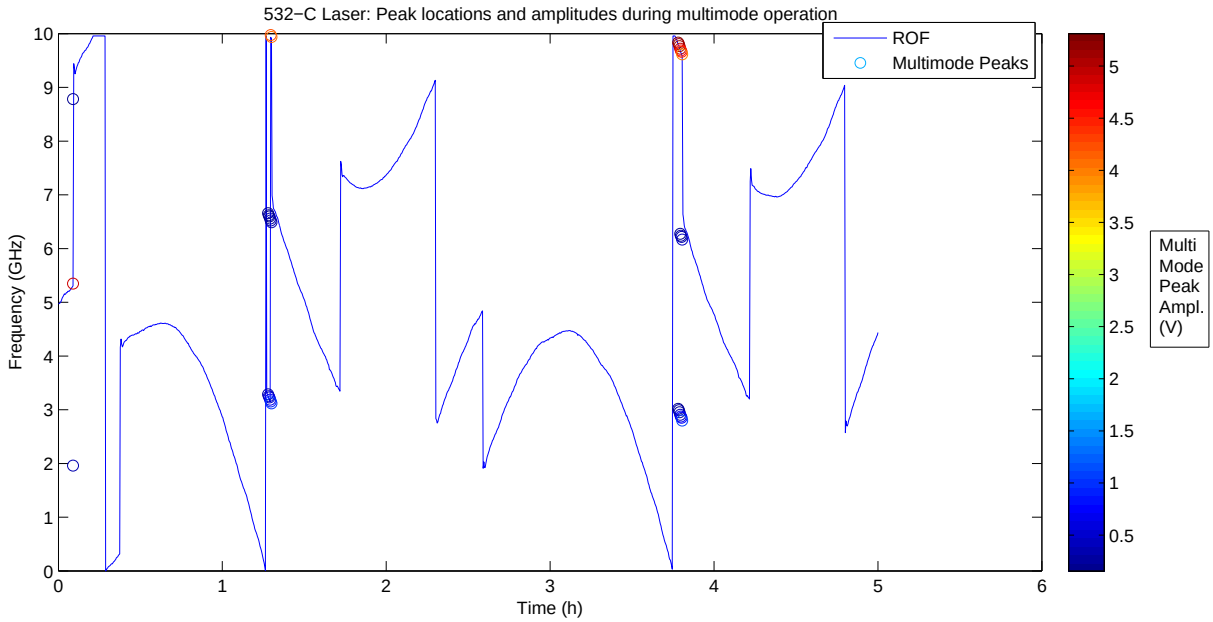

Figure 13: Multimode locations and amplitudes for 532-C laser (ID#23)

4.1.6 Noise in FPI data at low base plate temperatures for 532-R and 561-R lasers

During base plate temperature cycling, several of the R-lasers experienced frequency noise (0.1 - 0.5 GHz) when the base plate temperature was reduced to around 20-25$^{\circ}C$. A likely cause for the frequency noise is that the controlled temperature of TEC4 begins to fluctuate at low base plate temperatures. See figure 14 for an example of the phenomenon. The plot shows one laser with frequency noise of amplitude ~0.3 GHz, while the fluctuations in TEC temperature measure 0.08 $^{\circ}C$. Measurements on tuning of frequency by adjusting of TEC4 temperature (see section 4.3.2 for details) shows that $\frac{\Delta\nu}{\Delta T} \approx 4.5\,GHz/^{\circ}C$, meaning that TEC4 noise of 0.08$^{\circ}C$ could in fact result in frequency noise of ~0.36 GHz.

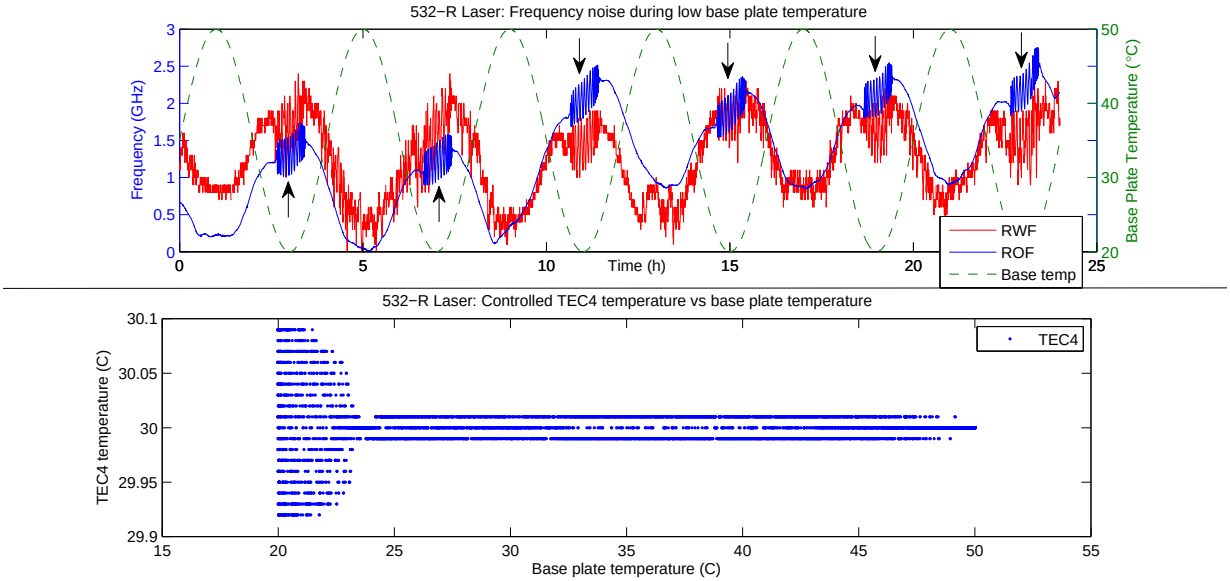

Figure 14: Plot of frequency noise during low base plate temperature for 05-laser (ID#:R3)

4.2 Constant base plate temperature measurements

Log files for the constant base plate temperature measurements were organized in the same way as for the base plate temperature cycle measurements:

- **Temperature cycle measurement log (TCM):** Time, Base plate temperature, Number of detected peaks, FPI frequency for largest peak, FPI amplitude for largest peak, temperature of internal TECs, WM frequency
- **Multi-peak Log (MP):** Time, Base plate temperature, FPI peak frequencies, FPI peak amplitudes

Using the TCM log it is possible to determine ROF and RWF, using the same definitions as for the base plate temperature cycle measurement. By observing RWF and ROF over time we can determine how much the frequency of the laser changes when base plate temperature is held constant and if any spontaneous mode jumps take place. Additionally the peak detection data of the FPI allows us to determine if the laser being tested can spontaneously experience multimode operation during constant base plate temperature.

4.2.1 Plots of frequency changes during constant base plate temperature of 35^oC

The two variables ROF & RWF can be plotted against time to illustrate frequency drift during constant base plate temperature. Examples of such plots can be seen for measurements on a 532-1 laser, a 561-1 laser, a 532-R laser and lastly a 561-R in figures 15, 16, 17 and 18.

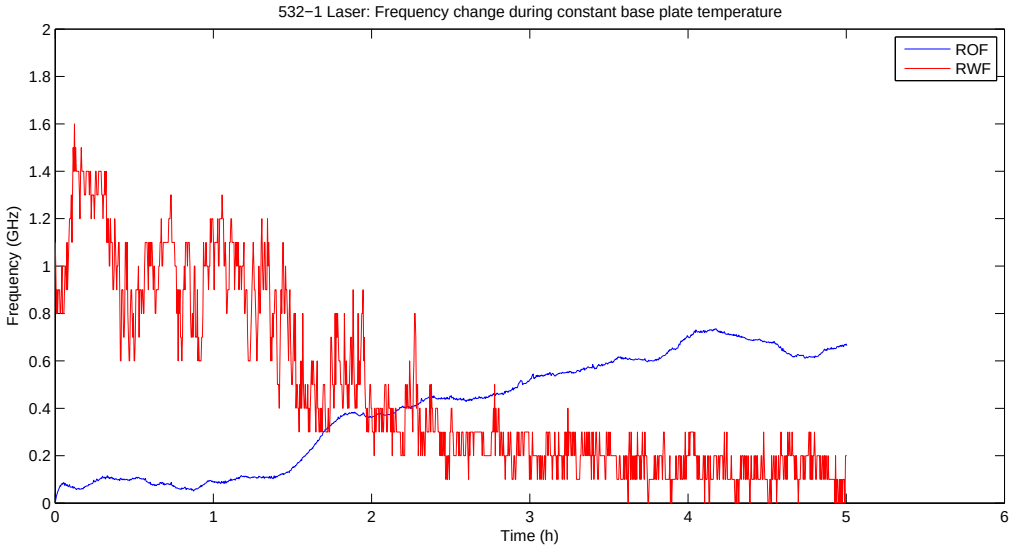

Figure 15: Plot of frequency change for a 532-1 laser during constant base plate temperature (ID#:3)

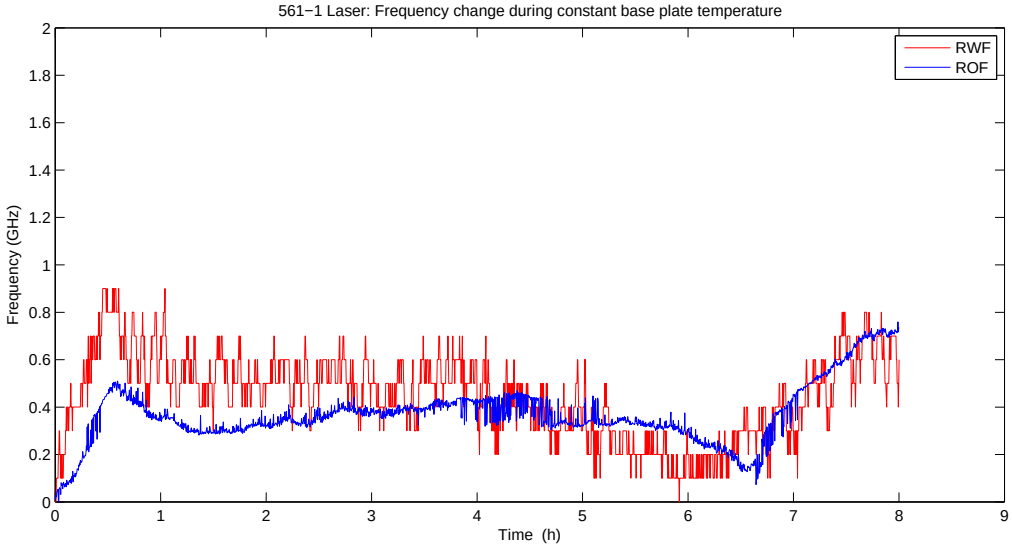

Figure 16: Plot of 561-1 laser frequency change during constant base plate temperature (ID#:17)

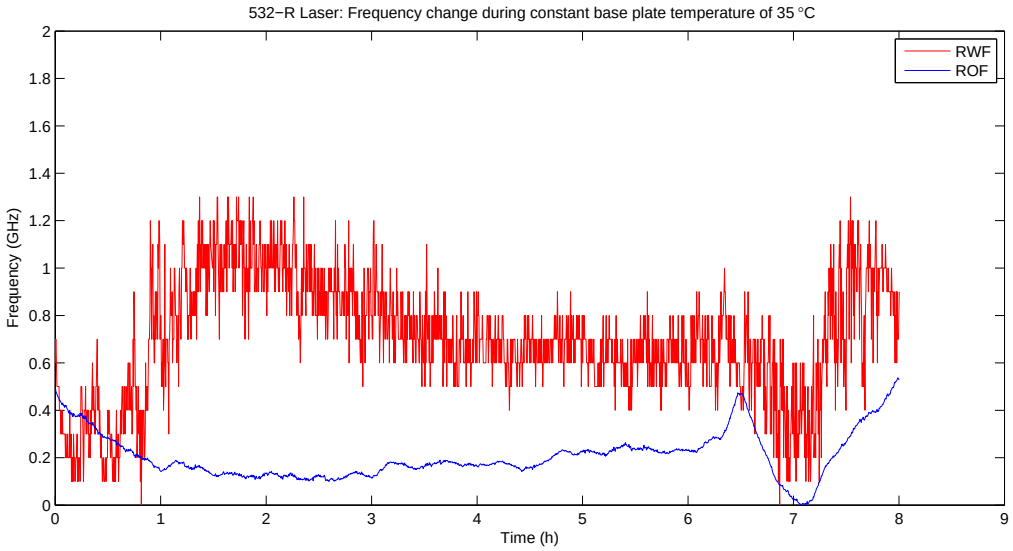

Figure 17: Plot of 532-R laser frequency change during constant base plate temperature (ID#:R5)

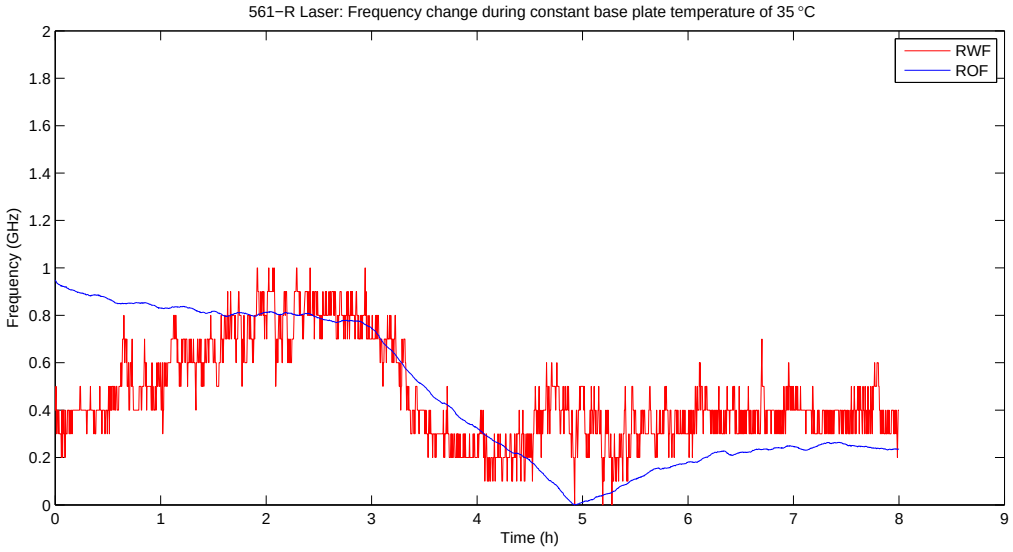

Figure 18: Plot of 561-R laser frequency change during constant base plate temperature (ID#:R7)

4.2.2 Tabulation of measurement results for constant base plate temperature

Based on FPI-, WM- and peak detection data a number of characteristic values were determined and tabulated:

ID#	Identification number for laser (ring cavity lasers begin ID# with R)
ROF_{max}	The highest value of ROF during the measurement; can indicate the span of frequencies measured by the FPI, but is limited to frequency spans $\leq$10 GHz.
RWF_{max}	The highest value of RWF during the measurement; indicating the span of frequencies measured by the WM.
# Jumps/hour	Mean number of mode jumps per hour of measurement.
Mean Jump Size	Large, discrete changes in frequency measured by WM are identified as mode jumps; the mean of the size of these jumps are then calculated.
Multimode %	Fraction of data points where detected peaks > 1. indicates how often the FPI registers multimode operation during measurement.

Model	ID #	P (mW)	ROF_{max} (GHz)	RWF_{max} (GHz)	# Jumps / h	Mean Jump Size (GHz)	Multimode %
532-1	1	50	2.9[a]	1.5	0	0	0
532-1	2	50	0.8	1.3	0	0	0
532-1	3	50	0.7	1.4	0	0	0
532-1	4	300	1	1.1	0	0	0
532-1	5	50	1.5	1.1	0	0	0
532-1	6	100	0.8	1	0	0	0
532-1	8	50	0.6	N/A	0	0	0
532-1	9	100	3.9[a]	2	0	0	0
532-1	10	300	0.4	N/A	0	0	0
532-1	11	100	3.2	7	1/20	6.8	0
532-1	12	100	3.9[a]	2	0	0	0
532-1	13	100	5.7[a]	1.1	0	0	0
532-1	14	50	6.2[a]	2.2	0	0	0
532-1	15	50	0.7	1.8	0	0	0
532-1	25	50	0.7	N/A	0	0	0
561-1	16	100	1.2	1.6	0	0	0
561-1	17	150	0.7	0.8	0	0	0
561-1	18	150	4.8[a]	1.6	0	0	0
561-1	19	100	5.9[a]	1.7	0	0	0
561-1	20	50	1.0	1.0	0	0	0
561-1	21	100	1.2	2.1	0	0	0
561-1	26	100	1.2	1.6	0	0	0
532-C	22	100	0.7	N/A	0	0	0
532-C	23	150	0.7	N/A	0	0	0
532-M	24	50	1.3	N/A	0	0	0

Table 3: Measurement results for standing wave lasers during constant base plate temperature

[a]FPI drifted significantly during the measurement, see 4.2.4 for details

Model	ID #	P (mW)	ROF_{max} (GHz)	RWF_{max} (GHz)	# Jumps / Cyc	Mean Jump Size (GHz)	Multimode %
532-R	R1	1000	0.8	1.1	0	0	0
532-R	R2	500	1.2	1.6	0	0	0
532-R	R3	1500	1.3	1.4	0	0	0
532-R	R4	1500	3.1[a]	1.6	0	0	0
532-R	R5	1500	0.5	1.2	0	0	0
561-R	R6	500	0.5	1.1	0	0	0
561-R	R7	500	0.9	0.9	0	0	0
561-R	R8	200	1.1	0.9	0	0	0
1064-M	R9	400	0.3	0.2	0	0	0

Table 4: Measurement results for unidirectional ring cavity lasers during constant base plate temperature

[a] FPI drifted significantly during the measurement, see 4.2.4 for details

4.2.3 A single mode jump during constant temperature

During a long test of a 532-1 with constant base plate temperature, a single spontaneous mode jump was detected measuring -7 GHz on the WM and +3 GHz on the FPI, suggesting that both picked up the same jump and that it was not a measurement error.

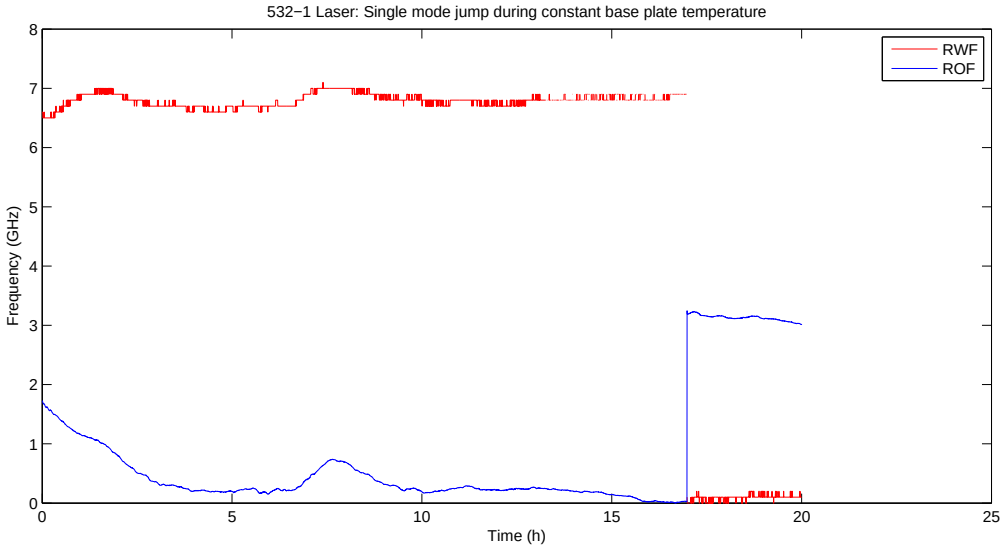

Figure 19: Single mode jump during constant base plate temperature cycling of 532-1 laser (ID#:11)

4.2.4 FPI frequency drifting relative to WM frequency

Occasionally during the constant base plate temperature measurements the FPI would measure a significant drift in frequency, while some much smaller disturbance was registered on the WM. A cause for this phenomenon was not determined, but the fact that some disturbance seemed to register on the WM while the FPI drifted suggests that it is not simply the result of changes in the FPI, but rather the result of some change in the setup, laser or surrounding environment (temperature, vibrations, power supply). See figure 20 for an example of one 561-1 laser experiencing this phenomenon several times during a long test (40 hours) at constant base plate temperature, performed over a weekend.

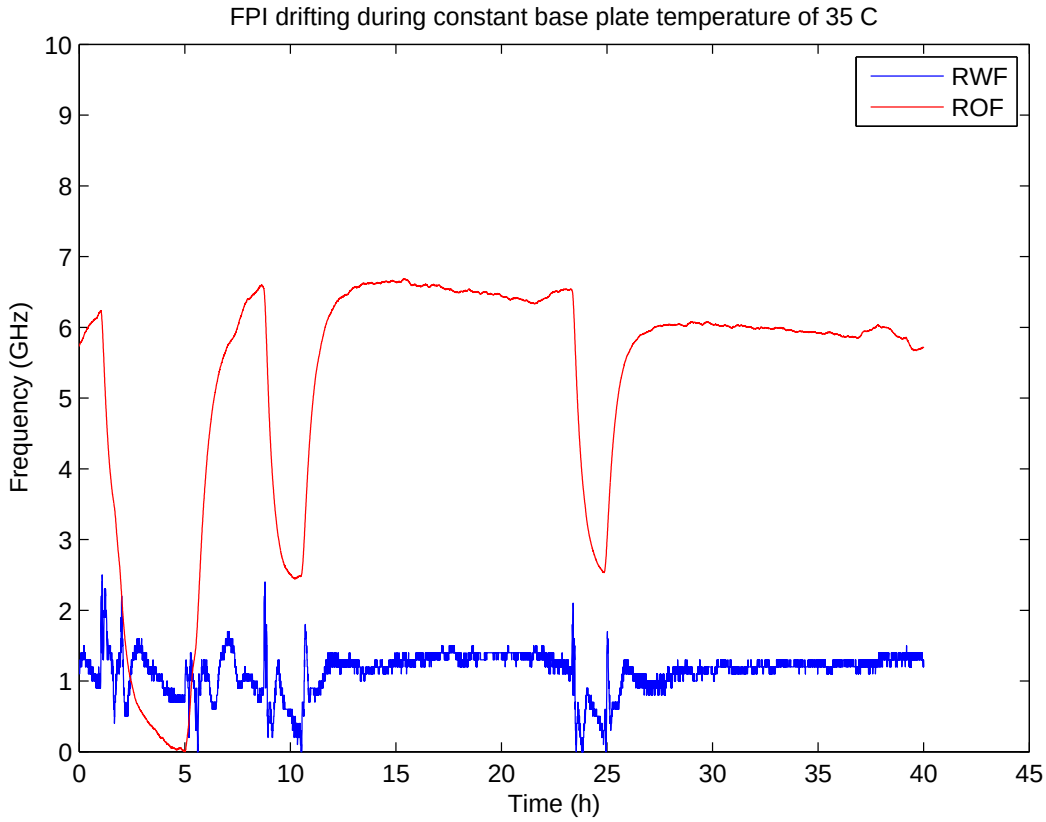

Figure 20: FPI drifting multiple times during constant base plate temperature test of a 561-1 laser (ID#:19)

4.3 Internal TEC temperature cycling

4.3.1 532-1 Laser TECs

Lyot Filter TEC (LF)

Tuning the LF-TEC on a 532-1 laser resulted in a large amount of mode jumps and tuning over a relatively large span of laser frequencies. Frequency tuning was almost exclusively stepwise; the result of mode jumps as the bandpass filter was tuned from mode to mode. See figure 21 for a plot displaying how frequency measured by the WM changed with time during temperature cycling. Additionally, see figure 22 for a plot displaying a linear fit for the tuning of frequency with changes in LF-TEC temperature.

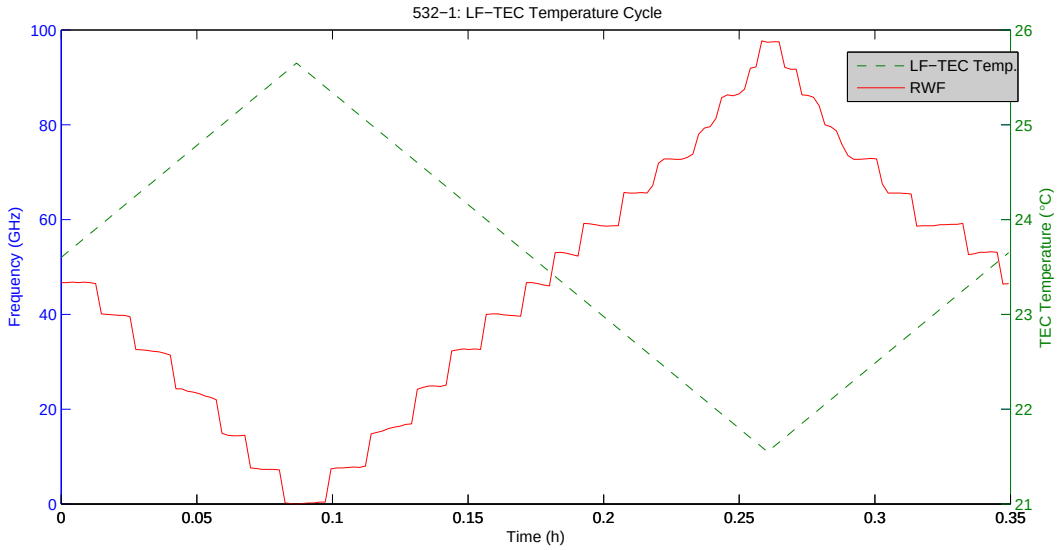

Figure 21: Frequency change during LF-TEC temperature cycling for a 532-1 laser (ID#:14)

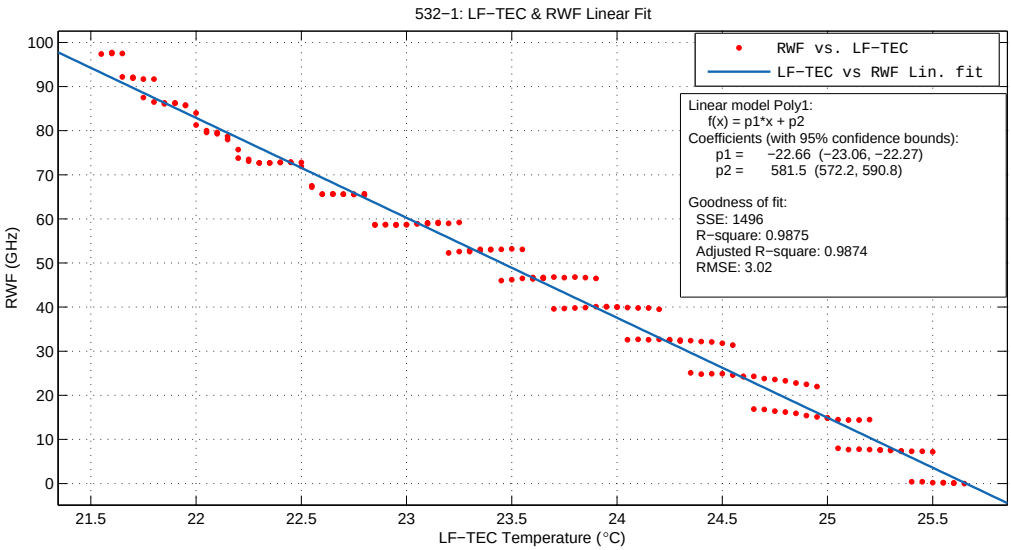

Figure 22: Plot of a linear fit for frequency tuning with LF-TEC temperature for a 532-1 laser (ID#:14)

Internal Base Plate TEC

Tuning the IBP-TEC on a 532-1 laser resulted in a roughly continuous, linear tuning of the laser frequency with a few mode jumps, likely as the mode became tuned off the frequency range of the band-pass filter. See figure 23 for a plot displaying the frequency change over time during temperature cycling of the IBP-TEC.

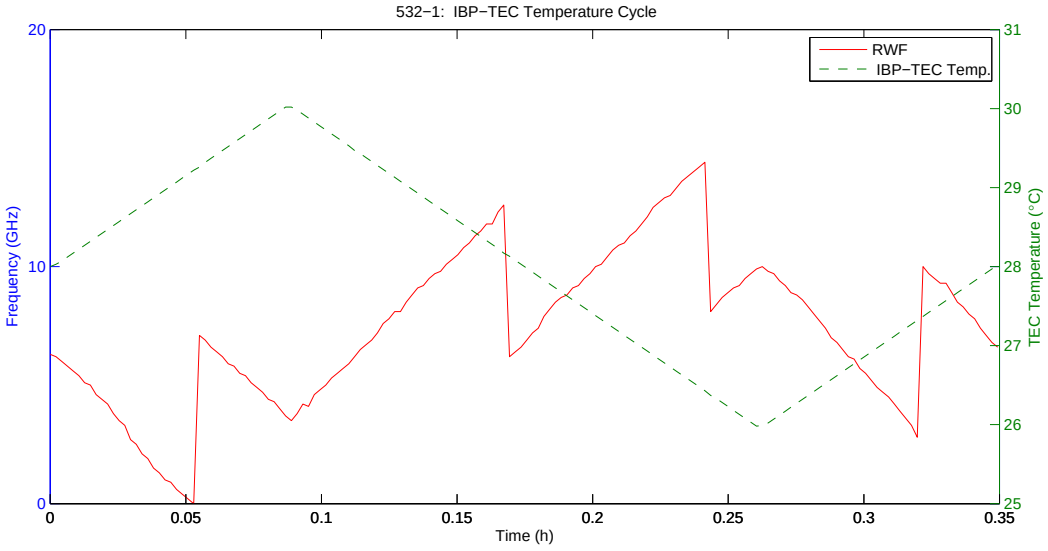

Figure 23: Plot of frequency change during IBP-TEC temperature cycling for a 532-1 laser (ID#:14)

4.3.2 532-R TECs

PP Crystal TEC (PPC)

Tuning TEC3 on a 532-R laser resulted in non-linear tuning of frequency. When TEC3 was raised above T_{start} the frequency was significantly tuned, while lowering TEC3 temperature below T_{start}had very little effect on frequency. See figure 24 for a plot of frequency change over time during temperature cycling of TEC3.

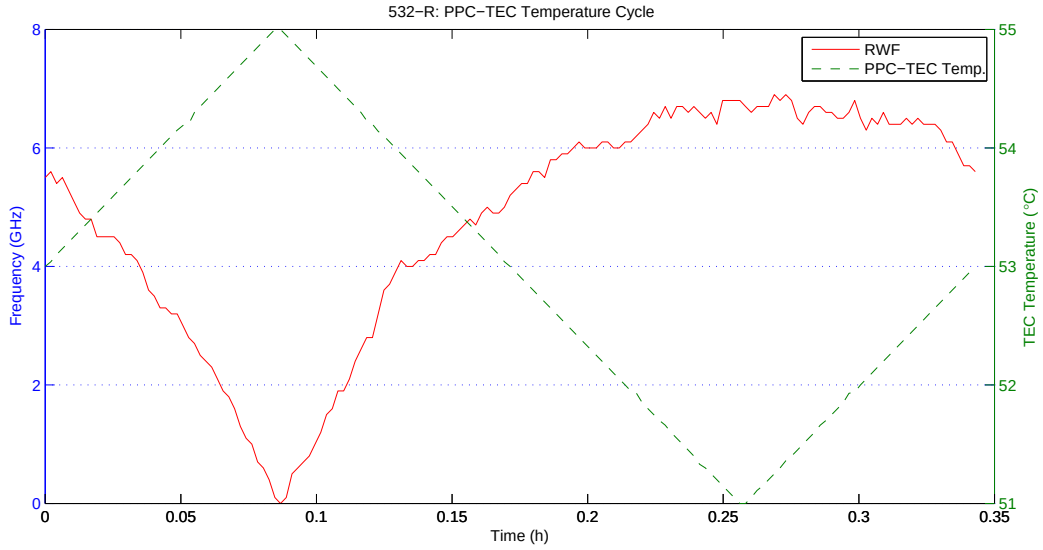

Figure 24: Plots of frequency change during PPC-TEC temperature cycle for a 532-R laser (ID#:R5)

Internal Base Plate TEC (IBP)

Tuning the IBP-TEC temperature resulted in a roughly linear tuning of frequency. See figure 25 for a plot of frequency change over time during temperature cycling of the IBP TEC. figure 26 is a plot of RWF values against IBP-TEC temperature values and includes a linear fit to the data.

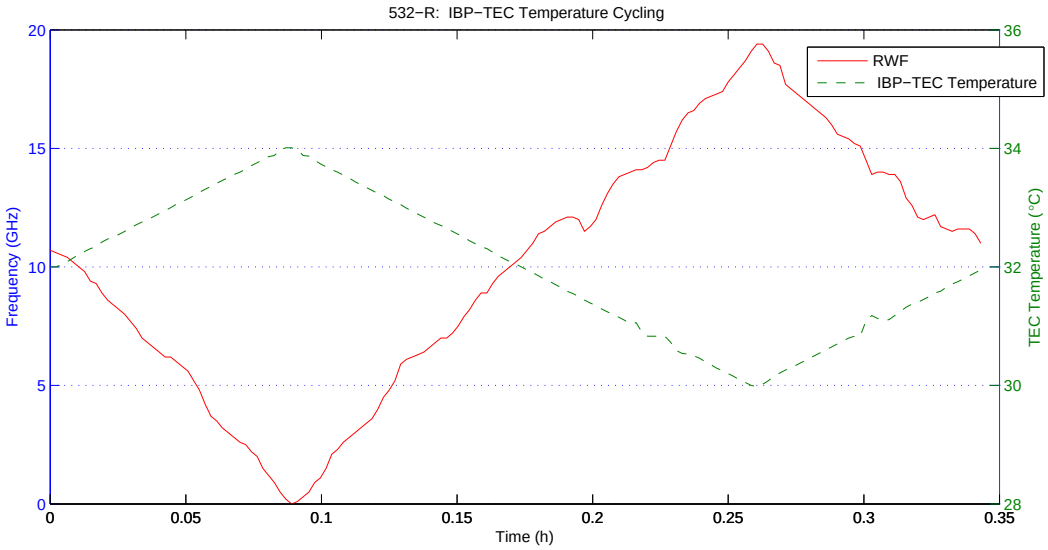

Figure 25: Plots of frequency change during IBP-TEC temperature cycle for a 532-R laser (ID#:R5)

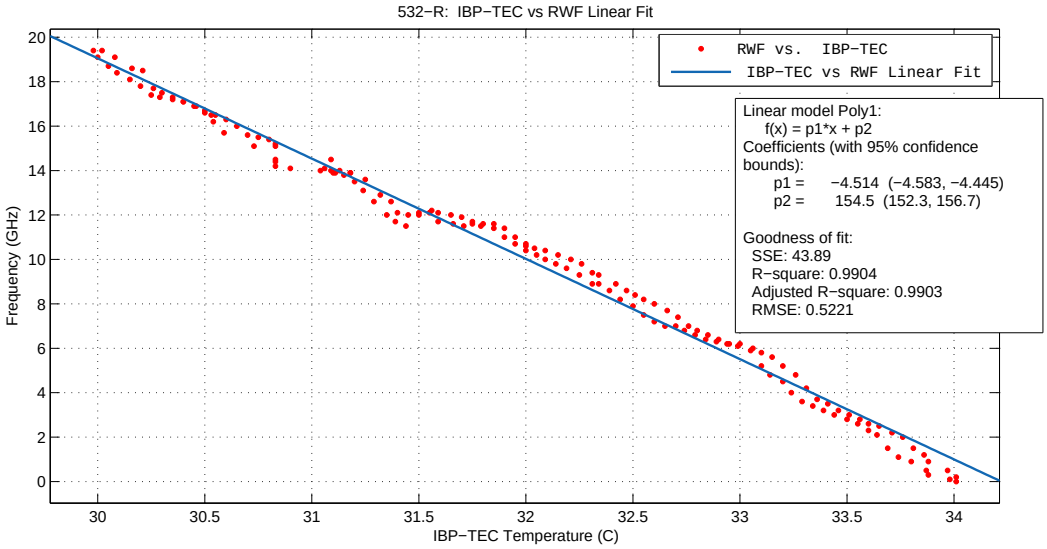

Figure 26: Plot of a linear fit for frequency tuning with IBP-TEC temperature for a 532-R laser (ID#:R5)

4.3.3 561-R TECs

Periodically Poled Crystal TEC (PPC)

Tuning of frequency with the PPC-TEC was distinctly non-linear for the 561-R, with large variation in frequency when TEC temperature was lowered below T_{start} and very little variation when raised above T_{start}. See figure 27 for a plot of frequency change over time during temperature cycling of the PPC-TEC.

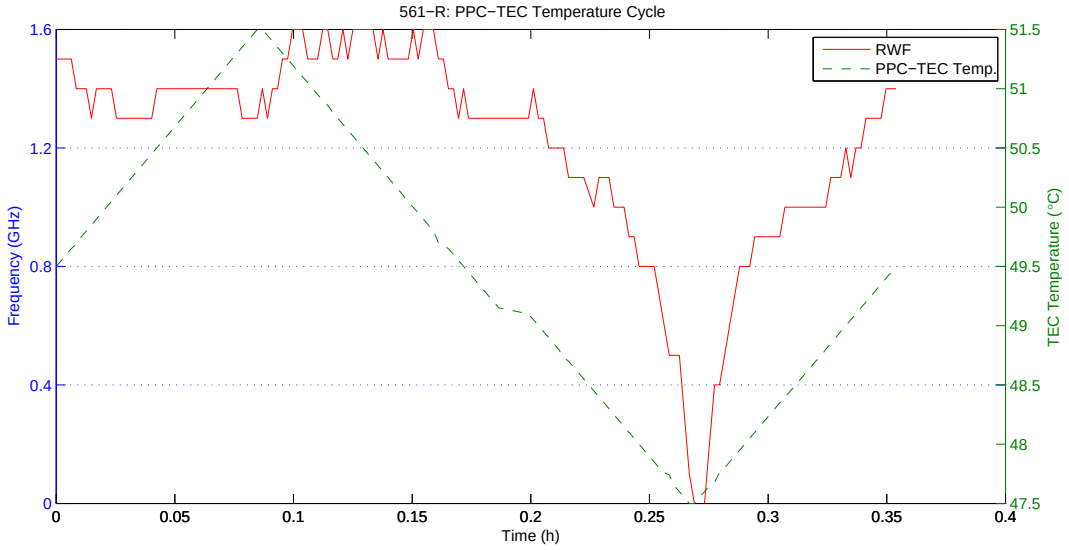

Figure 27: Plots of frequency change during PPC-TEC temperature cycle for a 561-R laser (ID#R8)

Internal Base Plate TEC (IBP)

Tuning IBP-TEC on a 561-R laser resulted in an approximately linear tuning of frequency, but with a single mode jump. See figure 28 for a plot of frequency change over time during temperature cycling of the IBP-TEC.

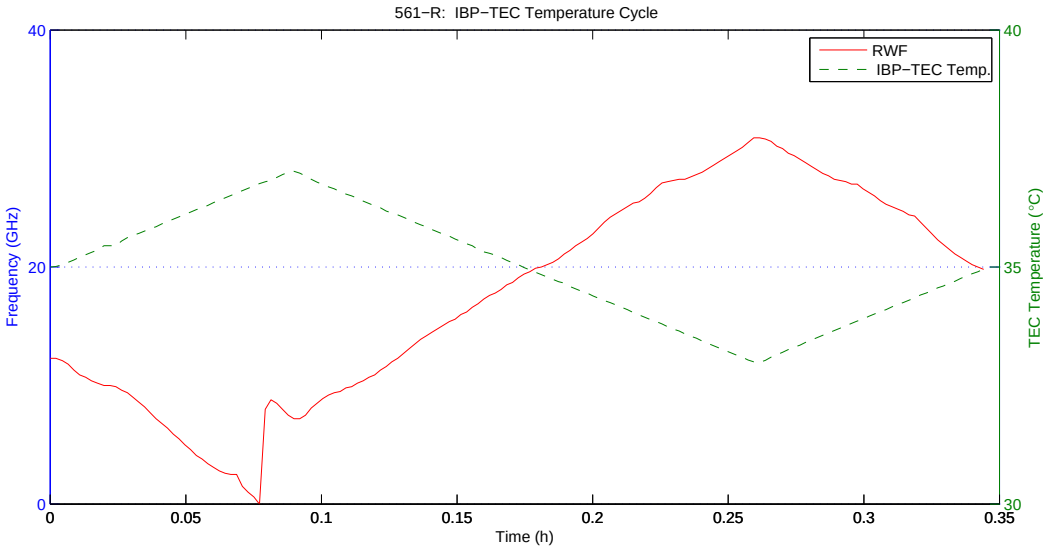

Figure 28: Plots of frequency change during IBP-TEC temperature cycle for a 561-R laser (ID#:R8)

4.3.4 532-M TECs

Lyot Filter TEC (LF)

Tuning the LF-TEC on 532-M laser caused tuning of the bandpass filter, resulting in large amounts of mode jumps and stepwise tuning of the laser frequency. See figure 29 for a plot of frequency changes over time during LF-TEC temperature cycling. figure 30 is a plot of the stepwise tuning of frequency with TEC temperature, and includes a linear fit to the data.

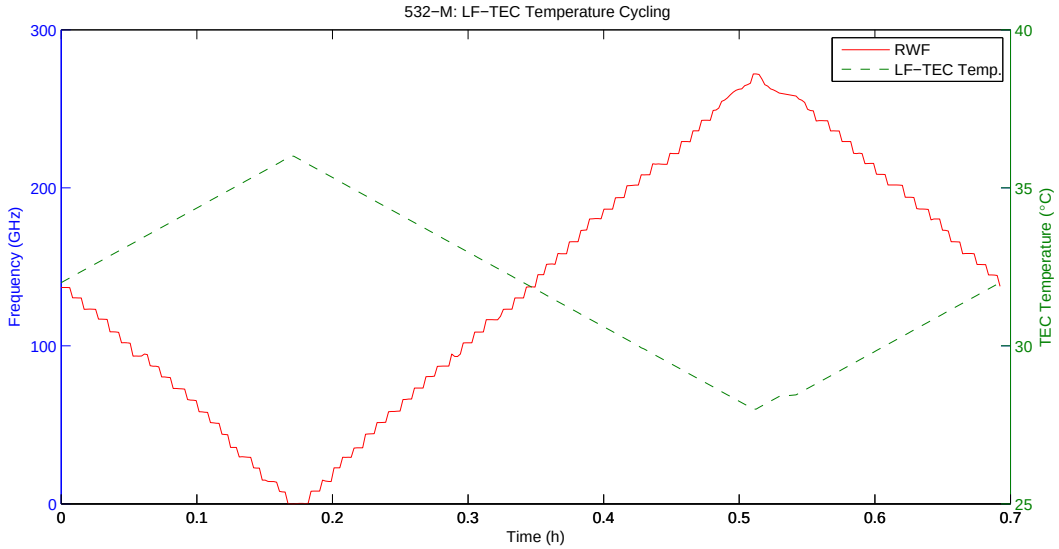

Figure 29: Plots of frequency change during LF-TEC cycling for a 532-M laser (ID#:24)

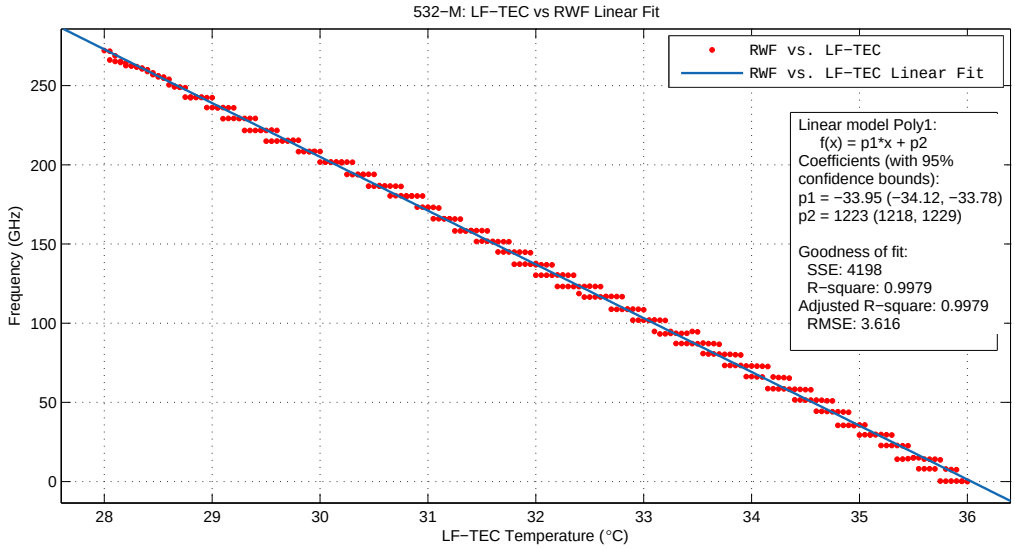

Figure 30: Plot of a linear fit for frequency tuning with LF-TEC temperature for a 532-M laser (ID#:24)

Internal Base Plate TEC (IBP)

Changes to the IBP-TEC temperature caused approximately linear tuning of output laser frequency, with a few mode jumps. See figure 29 for a plot of frequency change during a temperature cycling measurement of the IBP-TEC.

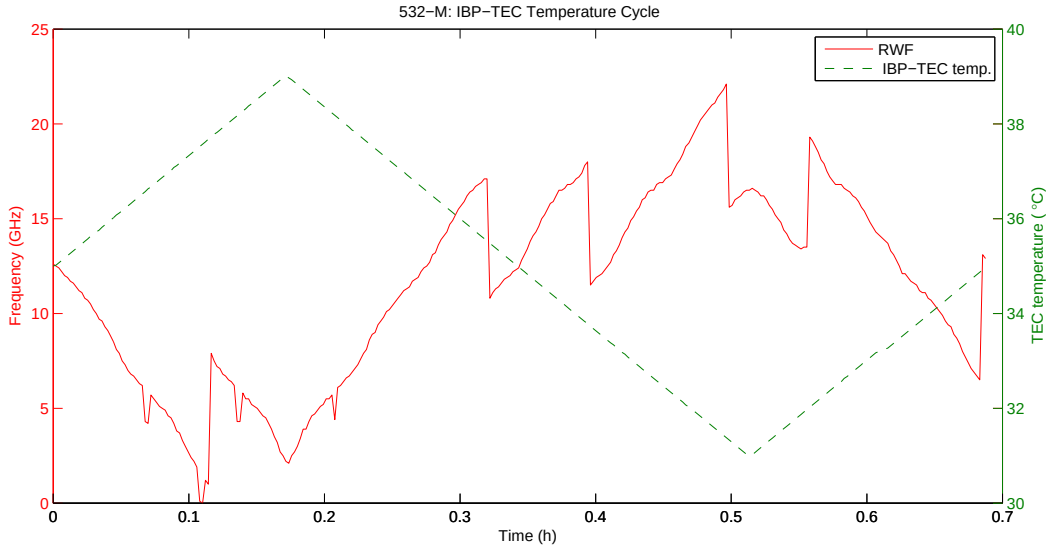

Figure 31: Plot of frequency change during IBP-TEC temperature cycling for a 532-M laser (ID#:24)

4.3.5 1064-M TEC

Internal Base Plate TEC (IBP)

Cycling the IBP-TEC temperature on the 1064-M laser resulted in linear tuning of output frequency, with mode jumps after approximately every 7 GHz of continuous frequency tuning. See figure 32 for a plot of the frequency change over time during the IBP-TEC temperature cycle measurement.

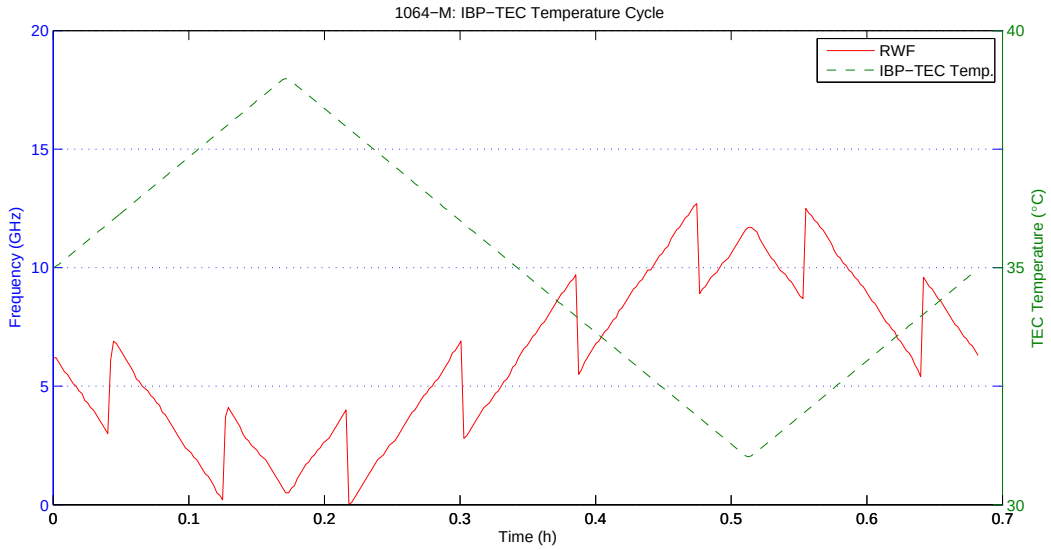

Figure 32: Plot of frequency change during temperature cycling of IBP-TEC for a 1064-M laser (ID#:R9)

4.3.6 Estimating $\Delta\nu/\Delta T_{TEC}$ at T_{start}

For each data point a differential was estimated using a simple two point estimation with $(\nu_i - \nu_{i-1})$ based on FPI peak data

$$[\frac{d\nu}{dT}]_i = \frac{(\nu_i - \nu_{i-1})}{(T_i - T_{i-1})}$$

Differentials between $(T_{start} - 0.5°\text{C})$ and $(T_{start} + 0.5°\text{C})$ were then averaged over, with outliers excluded, to arrive at the final estimate for $\Delta\nu/\Delta T_{TEC}$.

4.3.7 Tabulation of measurement results for internal TEC temperature cycling

ID#	Identification number for laser (ring cavity lasers begin ID# with R)
RWF_{max}	The highest value of RWF during the measurement; indicating the span of frequencies measured by the WM during TEC temperature cycling.
TEC Pos.	Position of the TEC: Internal Base Plate (IBP), Lyot filter (LF), PP-crystal (PPC),
T_{start}	Original setting for TEC; central temperature around which the TEC temperature is tuned.
ΔT	Amplitude of TEC temperature tuning.
# Jumps/Cycle	A count of the number of mode jumps observed over one TEC temperature cycle.
$\frac{\Delta\nu}{\Delta T_{TEC}}$ @ T_{start}	Estimated derivative $\Delta\nu/\Delta T_{TEC}$ around the TEC temperature set during production, T_{start}. See section 4.3.6 for details.
Linear Fit $\frac{\Delta\nu_{RWF}}{\Delta T_{TEC}}$	Derivative $\frac{\Delta\nu}{\Delta T}$ of a linear fit $\nu_{lin.fit} = (\frac{\Delta\nu}{\Delta T}) \cdot T_{TEC} + C$, fitted to RWF and TEC data
Multimode %	Fraction of data points where detected peaks > 1. indicates how often the FPI registers multimode operation during measurement.

Model	ID #	TEC Pos.	T_{start} ($^\circ C$)	ΔT ($^\circ C$)	RWF_{max} (GHz)	# Jumps / Cycle	$\frac{\Delta\nu}{\Delta T_{TEC}}$ @ T_{start} $(GHz/^\circ C)$	Linear Fit $\frac{\Delta\nu_{RWF}}{\Delta T_{TEC}}(\frac{GHz}{^\circ C})$	Multimode %
532-1	14	LF	23.6	2	97.7	28	1.5	-22.7	4
		IBP	28	2	14.4	4	-5.2	N/A	0
532-1	27	LF	47.4	2	167.7	39	-1.1	-43.7	20
		IBP	28.4	2	16.1	2	-5.3	N/A	0
532-1	25	IBP	31.3	4	17.3	7	-4.9	N/A	2
532-R	R5	PPC	53	2	6.9	0	-1.9	N/A	0
		IBP	32	2	19.4	0	-4.7	-4.5	0
561-R	R8	PPC	49.5	2	1.6	0	0.12	N/A	0
		IBP	35	2	30.9	1	-5.90	N/A	0
1064-M	R9	IBP	35	4	12.7	8	-3.6	N/A	0
532-M	24	LF	32	4	272.1	70	-0.9	-34.0	15
		IBP	35	4	16.7	6	-4.2	N/A	3

Table 5: Measurement results for internal TEC temperature cycling

5 Discussion of Results and Conclusions

5.1 Single mode operation

During constant base plate temperature all 30 lasers tested were found to oscillate on single longitudinal mode. When base plate temperature cycling was performed three 532-1 lasers as well as two 532-C lasers were found to momentarily output multiple modes, most commonly right before or after a mode jump. It should be noted that during measurements peak detection thresholds were set to ignore peaks with amplitudes weaker than approximately[3] -10 dB of the main peak amplitude (if the threshold was set lower, FPI noise would sometimes flood the peak data with false side peaks), and this presents a limitation to the findings of the SLM investigation.

5.2 Frequency stability

5.2.1 Frequency change over time with constant base plate temperature

During constant base plate temperature the wavemeter detected only minor fluctuations in frequency, around 1.5 GHz or less for all lasers, but for 8 of the 30 lasers the FPI detected drifts in frequency between 3-7 GHz. Because the drift only registers as a small amount of noise on the WM it is unclear if the drift occurs because of changes in the measurement setup or if some change is taking place in the laser.

5.2.2 Frequency changes with base plate temperature cycling

Frequency tuning with temperature $\Delta\nu/\Delta T$

The results of the base plate temperature cycling measurement seem to suggest that the packaging of the laser cavity is the main deciding factor for sensitivity to temperature change rather than cavity design. 532-1 lasers, 561-1 lasers and the 1064-M laser share similar values for estimated $\Delta\nu/\Delta T$ (0.5-0.7 GHz/°C) despite 532-1 and 561-1 being standing wave lasers while the 1064-M is a unidirectional ring cavity laser. It should be noted that if the 1064-M light (1064 nm) was frequency doubled before emission, the frequency tuning $\Delta\nu/\Delta T$ would be multiplied by a factor two resulting in a value 1.02 GHz/°C which is higher than the value measured for most 532-1 and 561-1 lasers, and coincides with the single outlier 532-1 laser (ID#:4) measuring 1.00 GHz/°C of tuning.

Laser models 532-R and 561-R both exhibit tuning values lower than 0.1 GHz/°C, demonstrating at least a factor 5 lower sensitivity to temperature change compared to 532-1 and 561-1 models. It is noteworthy that the 532-M laser seems to exhibit frequency tuning comparable to the -R lasers, despite sharing cavity design with the more sensitive -1 lasers.

The compact 532-C lasers seem to represent a middle ground in terms of frequency tuning, with $\Delta\nu/\Delta T$ values around 0.2 GHz/°C.

[3] For high powered lasers ($P \geq 500\,mW$) the FPI signal to noise ratio was far better, and peak threshold was commonly set close to -20 dB of main peak amplitude

Mode jumps

The size of mode jumps measured for the 532-1 lasers for the most part correspond well to the mode spacings calculated in section 2.5.1, suggesting that mode jumps in 532-1 lasers take place as a neighboring mode (with $\Delta\nu_{1064nm} \approx 3.3\,GHz$) experiences less gain than the current main mode, takes over, becomes frequency doubled and shifts output frequency by $2\Delta\nu_{1064nm} \approx 6.6\,GHz$. If the mode jumps only appeared as a result of main mode frequency being tuned off the bandpass filter, one would expect to see a relationship between the amount of frequency tuning and the number of mode jumps but looking at the results for temperature cycling of 532-1 lasers we see many lasers defy this trend. I.e the laser 532-1-ID#8 has the lowest measured value for $\Delta\nu/\Delta T$ at 0.34 GHz/°C and yet experiences the largest number of mode jumps during a base plate temperature cycle, at 12 jumps/cycle. This could indicate that some tuning of the bandpass filter is taking place during the base plate temperature cycle.

The measured mode jumps for 561-1 lasers suggest a more complicated process for frequency changes in 561-1 lasers. While some one the 561-1 lasers would repeatedly experience mode jumps around 10 GHz, close to the mode spacing predicted in section 2.5.1($2\Delta\nu_{1123nm} \approx 2 \times 4.5\,GHz \approx 9.0\,GHz$), many mode jumps measured ~15 GHz corresponding to roughly $3\Delta\nu_{1123nm}$. See figure 33 for an example of these mode jumps for a 561-1 laser(ID#17). It is not completly clear what would cause this variation in output mode jumps. If the jump resulted from sum frequency generation between two coexistent modes $(\nu_{1123nm} + \Delta\nu_{1123nm})$ and $(\nu_{1123nm} + 2\Delta\nu_{1123nm})$ one would expect to see additional output modes as a result of second harmonic generation at $2(\nu_{1123nm} + \Delta\nu_{1123nm})$ and $2(\nu_{1123nm} + 2\Delta\nu_{1123nm})$. During cooling of the 561-1 laser shown in figure 33 the WM not only measures larger mode jumps but also increased frequency tuning before the mode jump takes place, compared to frequency tuning during heating of the base plate. This would suggest that different changes to beam path takes place when cooling and heating. Perhaps the extra frequency jump during cooling is the result of mode jumps coinciding with some sudden change in cavity geometry that causes changes in beam path, I.e a snap movement of the bandpass filter components. The measured jump in frequency would then be a sum of the frequency change caused by cavity length change and longitudinal mode change.

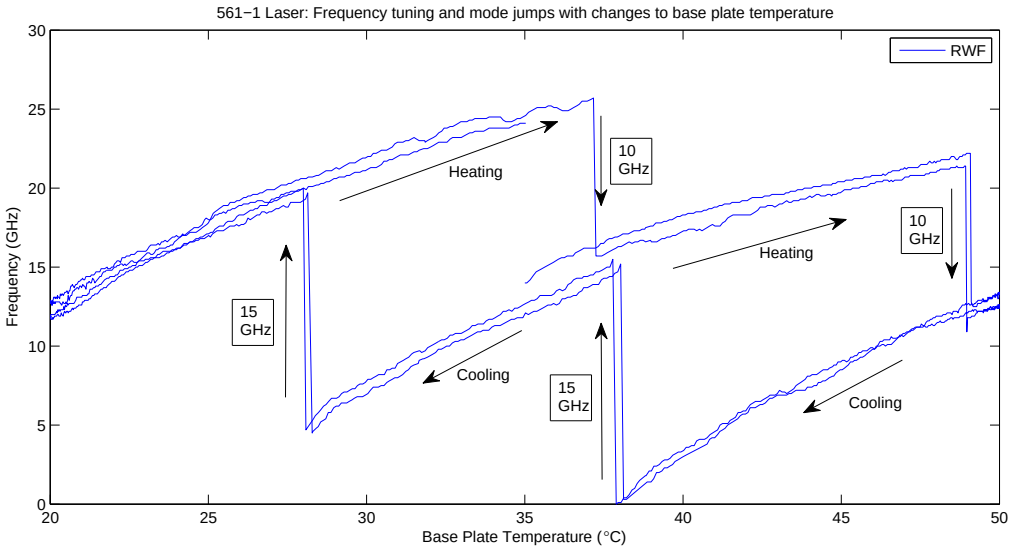

Figure 33: Plot showing varying tuning and mode jumps during heating and cooling of 561-1 laser (ID#:17)

It is interesting to note the mode jump behavior of the 1064-M laser as it exhibits a surprising tendency to mode jump, considering it is built as a unidirectional ring cavity laser. Only taking the external base plate temperature cycling measurements into account it is not possible to compare mode jumping in the 1064-M with 532-R and 561-R lasers, as the two latter have much less frequency tuning with external temperature change and thus do not run the risk of mode jumping. But observing the results of the internal base plate TEC (IBP-TEC) cycling measurements for the three lasers we can note that while the three lasers have comparable, linear tuning (see $\frac{\Delta\nu}{\Delta T_{TEC}}$column in table 5), the 1064-M still experienced more mode jumps. Even after taking into account the fact that the measurement for the 1064-M swept over twice the TEC interval, the laser still jumped 4 times more than the 561-R with similar tuning while the 532-R did not jump at all over comparable tuning ranges.

5.3 Possibility of compensating for frequency drift using internal TECs

5.3.1 532-1 & 532-M lasers

The characteristics of the LF-TECs & IBP-TECs is quite similar for the two models: The LF-TEC tuning causes stepwise tuning of frequency and seems mostly useful for large scale tuning in output frequency and for making adjustments to the spectral range of the bandpass filter. Nudging the bandpass filter with small changes to the LF-TEC could possibly be useful to prevent mode jumps and momentary multimode by making sure the filter is centered on the main mode. The IBP-TEC seems like the most promising candidate for counteracting small drifts in frequency, as frequency tuning with IBP-TEC temperature is mostly smooth and linear at ~5 GHz/°C.

5.3.2 532-R & 561-R lasers

The two ring cavity lasers seem to respond in similar fashion to tuning of the PPC-TECs and IBP-TECs: Some small amount of tuning of output frequency takes place when changing the temperature of the PPC-TEC, but even over a small temperature interval the tuning is distinctly non-linear. The IBP-TEC is far more reliable for tuning, with a roughly linear tuning of ~5 GHz/°C for both lasers.

5.3.3 1064-M laser

Only one internal TEC was available for tuning of the 1064-M, but the IBP-TEC did have good characteristics; continuous and linear tuning of frequency with TEC temperature.

6 Suggested work

6.1 Further investigation of SLM and internal TEC tuning

It is possible that if FPI noise in the waveform data was filtered away, one could lower the threshold for peak detection and potentially detect extremely weak side modes (smaller than -20 dB of the main mode). One way to achieve this would be to set the oscilloscope to average the trace over some time period, this has been shown to greatly reduce noise in the trace. Unfortunately the Labview VI used in this thesis to acquire waveform data does not appear to function when the oscilloscope is configured to average over time. Another option to deal with noise in the waveform data could

be to take the mean amplitude of several data points in the waveform data. The record length of the trace was set to 125k during the measurements of this thesis, but the oscilloscope used also supported record lengths of 1 million if one wanted more data points to average over, though this would possibly slow down the measurement loop considerably.

During the temperature cycling of internal TECs base plate temperature was kept at 35 °C, but by combining the functionality of the two test programs written for this thesis one could potentially change both base plate TEC temperature and internal TEC temperatures simultaneously, or set up automated tests investigate the how the characteristics of internal TEC tuning changes when base plate temperature was held constant at a set of different temperatures (I.e 20, 25, 30, 35, 40, 45 and 50 °C).

6.2 Implementing a controller using internal TECs to control output frequency

The results of the internal TEC temperature cycling showed that for all the lasers, the IBP-TEC could be used to continuously tune the output frequency. If one could determine the unwanted frequency drift one could potentially use that information to control the IBP-TEC temperature and counteract the drift. A FPI could be used to track drifts in frequency, although care would need to be taken to make sure the FPI does not drift without change in laser frequency (such as the drift seen in section 4.2.4). Counteracting the unwanted frequency drift using the IBP-TEC would not appear to assist in possible tuning of the bandpass filter, but for 532-1 lasers the LF-TEC is available to help counteract unwanted tuning of the bandpass filter. Determining that the mode was getting close to one of the ends of the bandpass filter would most likely require monitoring of laser current and laser power (measured by the built-in photodiode) to see when the mode begins to experience increased losses.

7 Appendix A

SVEA - Slowly-varying envelope approximation

The electric and polarization fields, propagating in x-direction inside a medium, can be expressed in term of their Forier components as

$E(x,t) = \frac{1}{2}[E(x,\omega)exp\,i(kx-\omega t)] + c.c.$

$P(x,t) = \frac{1}{2}[P(x,\omega)exp\,i(kx-\omega t)] + c.c.$

$E(x,\omega)$ and $P(x,\omega)$ are referred to as the envelope functions of the fields and express both phase and amplitude information about the propagating fields. If these envelopes vary slowly in both amplitude and phase with x and t then we can assume

$\left|\frac{\partial^2 E(\omega)}{\partial x^2}\right| \ll \left|k\frac{\partial E(\omega)}{\partial x}\right|$

$\left|\frac{\partial E(\omega)}{\partial t}\right| \ll |\omega E(\omega)|$

$\left|\frac{\partial^2 P(\omega)}{\partial t^2}\right| \ll \left|\omega\frac{\partial P(\omega)}{\partial t}\right| \ll |\omega^2 P(\omega)|$

This is known as the slowly-varying envelope approximation.

8 References

1. *106.5 W high beam quality diode-side-pumped Nd:YAG laser at 1123 nm*: Chaoyang L, Yong B, Feng Y, Zhichao W, Yiting X, Yuanbin W, Hongwei G, Qinjun P, Dafu C, Zuyan X. 2010. Optics Express Vol. 18, Issue 8

2. *Laser Diode pumped Nd:YAG Laser*: Edgar A. Peralta, Chunjin Jia, and Chenchen Wang. 2010. Stanford University

3. *Sellmeier and thermo-optic dispersion formulas for KTP*: K. Kato, E. Takaoka. 2002. Applied Optics Vol. 41, No. 24

4. *Nanosecond optical parametric oscillators and amplifiers based on periodically poled KTiOPO4*: Jonas Hellström. 2001. Doctoral thesis. KTH

5. *Principles of Lasers 4:th Ed.*: Orazio Svelto. Translated by David C. Hanna. 1998. Springer

6. *Handbook of Nonlinear Optics 2:nd Ed.*: Richard L. Sutherland. 2003, Marcel Dekker

7. *Laser Fundamentals 2:nd Ed.*: William T. Silfvast. 2004. Cambridge University Press

8. *The Elements of Nonlinear Optics*: P.N. Butcher, D. Cotter. 1990. Cambridge University Press